

# Revealing the structure of light pseudoscalar mesons at the Electron-Ion Collider

**J Arrington<sup>1</sup>, C Ayerbe Gayoso<sup>2</sup>, PC Barry<sup>6,21</sup>, V Berdnikov<sup>3</sup>,  
D Binosi<sup>4</sup>, L Chang<sup>5</sup>, M Diefenthaler<sup>6</sup>, M Ding<sup>4</sup>, R Ent<sup>6</sup>,  
T Frederico<sup>7</sup>, Y Furletova<sup>6</sup>, TJ Hobbs<sup>6,8,20</sup>, T Horn<sup>3,6,\*</sup>,  
GM Huber<sup>9</sup>, SJD Kay<sup>9</sup>, C Keppel<sup>6</sup>, H-W Lin<sup>10</sup>, C Mezrag<sup>11</sup>,  
R Montgomery<sup>12</sup>, IL Pegg<sup>3</sup>, K Raya<sup>5,13</sup>, P Reimer<sup>14</sup>,  
DG Richards<sup>6</sup>, CD Roberts<sup>15,16</sup>,  
J Rodríguez-Quintero<sup>17</sup>, D Romanov<sup>6</sup>, G Salmè<sup>18</sup>, N Sato<sup>6</sup>,  
J Segovia<sup>19</sup>, P Stepanov<sup>3</sup>, AS Tadepalli<sup>6</sup> and RL Trotta<sup>3</sup>**

<sup>1</sup> Lawrence Berkeley National Laboratory, Berkeley, CA 94720, USA

<sup>2</sup> Mississippi State University, Starkville, MS, USA

<sup>3</sup> Catholic University of America, Washington, DC, USA

<sup>4</sup> European Centre for Theoretical Studies in Nuclear Physics and Related Areas (ECT\*) and Fondazione Bruno Kessler Villa Tambosi, Strada delle Tabarelle 286, I-38123 Villazzano (TN) Italy

<sup>5</sup> School of Physics, Nankai University, Tianjin 300071, China

<sup>6</sup> Thomas Jefferson National Accelerator Facility, Newport News, Virginia 23606, USA

<sup>7</sup> Instituto Tecnológico de Aeronáutica, 12.228-900 São José dos Campos, Brazil

<sup>8</sup> Southern Methodist University, Dallas, TX 75275-0175, USA

<sup>9</sup> University of Regina, Regina, SK S4S 0A2, Canada

<sup>10</sup> Michigan State University, East Lansing, MI 48824, USA

<sup>11</sup> IRFU, CEA, Université Paris-Saclay, F-91191 Gif-sur-Yvette, France

<sup>12</sup> SUPA School of Physics and Astronomy, University of Glasgow, Glasgow G12 8QQ, United Kingdom

<sup>13</sup> Instituto de Ciencias Nucleares, Universidad Nacional Autónoma de México, Apartado Postal 70-543, C.P. 04510, CDMX, México

<sup>14</sup> Argonne National Laboratory, Lemont, IL 60439, USA

<sup>15</sup> School of Physics, Nanjing University, Nanjing, Jiangsu 210093, China

<sup>16</sup> Institute for Nonperturbative Physics, Nanjing University, Nanjing, Jiangsu 210093, China

<sup>17</sup> Department of Integrated Sciences and Center for Advanced Studies in Physics, Mathematics and Computation, University of Huelva, E-21071 Huelva, Spain

<sup>18</sup> Istituto Nazionale di Fisica Nucleare, Sezione di Roma, P.le A. Moro 2, I-00185 Rome, Italy

<sup>19</sup> Departamento de Sistemas Físicos, Químicos y Naturales, Universidad Pablo de Olavide, E-41013 Sevilla, Spain

<sup>20</sup> Department of Physics, Illinois Institute of Technology, Chicago, IL 60616, USA

<sup>21</sup> North Carolina State University, Raleigh, NC 27607, USA

E-mail: \*hornt@cua.edu

2021 January

<https://orcid.org/0000-0002-0702-1328> - J. Arrington  
<https://orcid.org/0000-0001-8640-5380> - C. Ayerbe Gayoso  
<https://orcid.org/0000-0001-6933-9166> - PC Barry  
<https://orcid.org/0000-0003-4916-6194> - VV Berdnikov  
<https://orcid.org/0000-0003-1742-4689> - D Binosi  
<https://orcid.org/0000-0002-4339-2943> - L Chang  
<https://orcid.org/0000-0002-4717-4484> - M Diefenthaler  
<https://orcid.org/0000-0002-3690-1690> - M Ding  
<https://orcid.org/0000-0001-7015-2534> - R Ent  
<https://orcid.org/0000-0002-5497-5490> - T Frederico  
<https://orcid.org/0000-0001-9032-1999> - Y Furltova  
<https://orcid.org/0000-0002-2729-0015> - TJ Hobbs  
<https://orcid.org/0000-0003-1925-9541> - T Horn  
<https://orcid.org/0000-0002-5658-1065> - GM Huber  
<https://orcid.org/0000-0002-8855-3034> - SJD Kay  
<https://orcid.org/0000-0002-7516-8292> - C Keppel  
<https://orcid.org/0000-0002-0899-3866> - HW Lin  
<https://orcid.org/0000-0001-8678-4085> - C Mezrag  
<https://orcid.org/0000-0002-2007-6833> - R Montgomery  
<https://orcid.org/0000-0002-1195-3013> - IL Pegg  
<https://orcid.org/0000-0001-8225-5821> - K Raya  
<https://orcid.org/0000-0002-0301-2176> - P Reimer  
<https://orcid.org/0000-0002-2937-1361> - CD Roberts  
<https://orcid.org/0000-0002-1651-5717> - J Rodríguez-Quintero  
<https://orcid.org/0000-0001-6715-3448> - D Romanov  
<https://orcid.org/0000-0002-9209-3464> - G Salmè  
<https://orcid.org/0000-0002-1535-6208> - N Sato  
<https://orcid.org/0000-0001-5838-7103> - J Segovia  
<https://orcid.org/0000-0002-0806-1743> - P Stepanov  
<https://orcid.org/0000-0002-5312-8943> - AS Tadepalli  
<https://orcid.org/0000-0002-8193-6139> - RL Trotta

**Abstract.**

How the bulk of the Universe’s visible mass emerges and how it is manifest in the existence and properties of hadrons are profound questions that probe into the heart of strongly interacting matter. Paradoxically, the lightest pseudoscalar mesons appear to be the key to the further understanding of the emergent mass and structure mechanisms. These mesons, namely the pion and kaon, are the Nambu-Goldstone boson modes of QCD. Unravelling their partonic structure and the interplay between emergent and Higgs-boson mass mechanisms is a common goal of three interdependent approaches – continuum QCD phenomenology, lattice-regularised QCD, and the global analysis of parton distributions – linked to experimental measurements of hadron structure. Experimentally, the foreseen electron-ion collider will enable a revolution in our ability to study pion and kaon structure, accessed by scattering from the “meson cloud” of the proton through the Sullivan process. With the goal of enabling a suite of measurements that can address these questions, we examine key reactions to identify the critical detector system requirements needed to map tagged pion and kaon cross sections over a wide range of kinematics. The excellent prospects for extracting pion structure function and form factor data are shown, and similar prospects for kaon structure are discussed in the context of a worldwide programme. Successful completion of the programme outlined herein will deliver deep, far-reaching insights into the emergence of pions and kaons, their properties, and their role as QCD’s Goldstone boson modes.

**Keywords:** electromagnetic form factors – elastic and transition; electron ion collider; emergence of mass; Nambu-Goldstone modes – pions and kaons; parton distributions; strong interactions in the standard model of particle physics

Submitted to: *J. Phys. G: Nucl. Part. Phys.*

## 1. Introduction

### 1.1. Mass budgets

The Standard Model has two mechanisms for mass generation. One is connected with the Higgs boson [1], discovered at the large hadron collider in 2012 [2, 3]. In the context of strong interactions, the Higgs produces the Lagrangian current-mass for each of the quarks. Yet, regarding the kernels of all known nuclei, these current masses account for less than 2% of the mass of a neutron or proton. More than 98% of visible mass emerges as a consequence of strong interactions within QCD [4–6]: this is emergent hadronic mass (EHM).

Consider, therefore, the Lagrangian of QCD in the absence of Higgs couplings to the quarks. Classically, it defines a scale invariant theory; and scale invariant theories do not support dynamics. Therefore, bound states are impossible and the Universe cannot exist.

The process of renormalisation in the quantisation of chromodynamics introduces a mass which breaks the scale invariance of the classical theory. Hence, in the absence of quark couplings to the Higgs boson, i.e. in the chiral limit, the QCD stress-energy tensor,  $T_{\mu\nu}$ , exhibits a trace anomaly [7]:

$$T_{\mu\mu} = \beta(\alpha(\zeta)) \frac{1}{4} G_{\mu\nu}^a G_{\mu\nu}^a =: \Theta_0, \quad (1)$$

where  $\beta(\alpha(\zeta))$  is QCD's  $\beta$ -function,  $\alpha(\zeta)$  is the associated running-coupling,  $G_{\mu\nu}^a$  is the gluon field strength tensor, and  $\zeta$  is the renormalisation scale. The consequences of equation (1) are wide-ranging and heavy in impact.

A first question to ask is whether the magnitude of  $\Theta_0$  can be measured and understood. Measurement is straightforward. Consider the following in-proton expectation value:

$$\langle p(P) | T_{\mu\nu} | p(P) \rangle = -P_\mu P_\nu, \quad (2)$$

where the equations-of-motion for a one-particle proton state produce the right-hand-side. In the chiral limit

$$\langle p(P) | T_{\mu\mu} | p(P) \rangle = -P^2 = m_p^2 = \langle p(P) | \Theta_0 | p(P) \rangle. \quad (3)$$

As highlighted by the blue domain in figure 1A, this expectation value is 94% of the proton's measured mass. Since  $\Theta_0$  is expressed solely in terms of gluons when a (large- $\zeta$ ) parton basis is used, then one might conclude that the chiral-limit value of  $m_p$  is generated completely by glue.

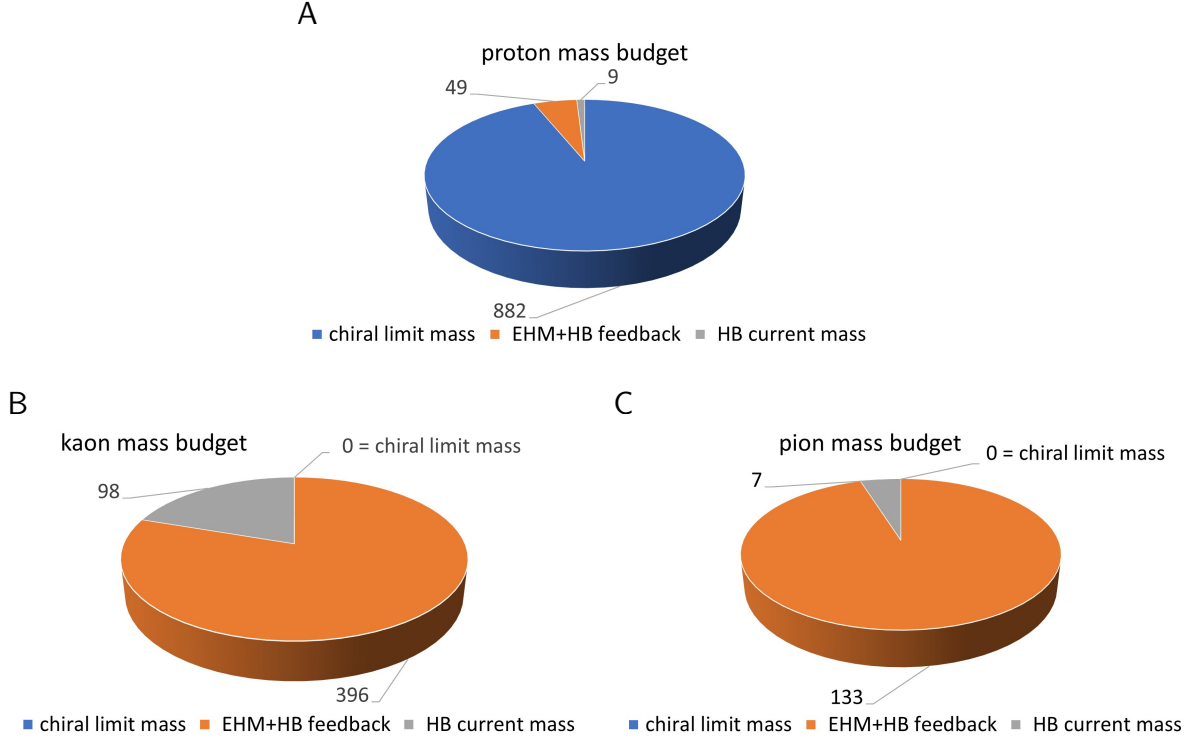


Figure 1: Mass budgets for the proton – A, kaon – B and pion – C. The differences are stark. Owing to EHM, the proton’s mass is large in the chiral limit. Conversely and yet still owing to EHM via its corollary dynamical chiral symmetry breaking, the kaon and pion are massless in the absence of quark couplings to the Higgs boson. (Units MeV, Poincaré-invariant separation at  $\zeta = 2 \text{ GeV}$ , breakdowns produced using information from [8, 9].)

However complex that might seem, Nature is even more subtle. This may be seen by returning to equation (2) and replacing the proton by the pion

$$\langle \pi(q) | T_{\mu\nu} | \pi(q) \rangle = -q_\mu q_\nu \quad \Rightarrow \quad \langle \pi(q) | \Theta_0 | \pi(q) \rangle = m_\pi^2 \stackrel{\text{chiral limit}}{=} 0 \quad (4)$$

because the chiral-limit pion is a massless Nambu–Goldstone (NG) mode [10, 11]. This feature is highlighted by the complete absence of a blue domain for the pion in figure 1C. Conceivably, this could mean that the scale anomaly is trivially zero in the

pion; to wit, strong gluon-gluon interactions have no effect in the pion because each term required to express  $\Theta_0$  vanishes separately [12]. However, such an explanation would sit uncomfortably with known QCD dynamics, which expresses both attraction and repulsion, often remarkable fine tuning, but never inactivity. (Additional discussion of these points may be found, e.g. in [4, section V], [5, sections 4.4, 4.5]).

Switching on the Higgs boson couplings to light quarks, then one encounters the other two wedges in figure 1A: grey shows the sum of Higgs-generated valence-quark current-masses in the proton, which amounts to just  $0.01 \times m_p$ ; and orange indicates the contribution generated by constructive interference between EHM and Higgs-boson (HB) effects, 5%. Again, the picture for the pion is completely different, with EHM+HB interference being responsible for 95% of the pion's mass. The kaon lies somewhere between these extremes. It is a would-be Nambu-Goldstone mode, so there is no blue-domain in figure 1B; but the sum of valence-quark and valence-antiquark current-masses in the kaon amounts to 20% of its measured mass – four times more than in the pion, with EHM+HB interference producing 80%.

Equations (3), (4), and the mass budgets drawn in figure 1 demand interpretation. They stress that any explanation of the proton's mass is incomplete unless it simultaneously clarifies equation (4). Moreover, both phenomena are coupled with confinement, which is fundamental to the proton's stability. These remarks highlight the ubiquitous influence of EHM. They emphasise that in order to finally complete the Standard Model, it is crucial to understand the emergence of mass within the strong interaction and the modulating effects of Higgs boson mass generation, both of which are fundamental to understanding the evolution of our Universe.

In facing these questions, unique insights can be drawn by focusing on the properties of QCD's (pseudo-)Nambu-Goldstone modes, i.e. pions and kaons; and diverse phenomenological and theoretical approaches are now being deployed in order to develop a coherent image of these bound states. Complete understanding demands that tight links be drawn between dynamics in QCD's gauge sector and pion and kaon light-front wave functions, and from there to observables, such as pion and kaon elastic form factors and distribution amplitudes and functions. Herein, we propose an array of measurements and associated analyses designed to deliver significant progress toward these goals [13, 14].

It is worth remarking here that *measurements* of form factors, distribution amplitudes and functions, spectra, charge radii, etc., are all on the same footing. Theory supplies predictions for such quantities. Experiments measure precise cross

sections; and cross-sections are expressed, via truncations that optimally have the quality of approximations, in terms of the desired quantity. At question is the reliability of the truncation/approximation employed in relating the measured cross section to this quantity. The phenomenology challenge is to ensure that every contribution known to have a material effect is included in building the bridge. The quality of the phenomenology can alter neither that of the experiment nor the theory. However, inadequate phenomenology can deliver results that mislead interpretation. The reverse is also true. Thus, progress requires the building of a positive synergy between all subbranches of the programme.

### *1.2. EIC context*

The electron-ion collider (EIC) [15] will be capable of addressing an array of profound questions that probe into the heart and reach out to the frontiers of strong interactions within the Standard Model. Looming large in this array are the emergence of the bulk of visible mass and its manifestations in the existence and properties of hadrons and nuclei. The research described herein aims to build a path toward answers by focusing on the properties of pions and kaons, the Standard Model's would-be Nambu-Goldstone modes. It combines experiment, phenomenology and theory in a synergistic effort to reveal: how the roughly 1 GeV mass-scale that characterises atomic nuclei appears; why it has the observed value; why ground-state pseudoscalar mesons are unnaturally light in comparison; and the role of the Higgs boson in forming hadron properties.

The focus on pions and kaons acknowledges that these states are unique expressions of Standard Model dynamics, exhibiting a peculiar dichotomy. Namely, they are hadron bound states defined, like all others, by their valence quark and/or antiquark content, making calculation of their properties no different, in principle, from proton computations; but the mechanism(s) which give all other hadrons their roughly 1 GeV mass-scale are obscured in these systems. This elevates studies of pion and kaon structure to the highest levels of importance. Yet, although discovered more than seventy years ago [16, 17], remarkably little is known about their structure. The EIC, with its high-luminosity and wide kinematic range, offers an extraordinary new opportunity to eliminate that ignorance. There is much to be learnt: pions and kaons are not pointlike; their internal structure is more complex than is usually imagined; and the properties of these nearly-massless strong-interaction composites provide the clearest windows onto EHM and its modulation by Higgs-boson interactions.

This report identifies a raft of measurements and associated phenomenology and theory that will exploit the distinctive strengths of the EIC in driving toward answers to some of the most basic questions in Nature. Successful completion of the programme will deliver deep, far-reaching insights into the distributions and apportionment of mass and spin within the pion and kaon; the similarities and differences between such distributions in these (almost) Nambu-Goldstone modes and the benchmark proton; the symbiotic relationship between EHM and confinement; and the character and consequences of constructive interference between the Standard Model's two mass-generating mechanisms.

## 2. Meson structure as a QCD laboratory - status and prospects

### 2.1. Pion and kaon structure - theory status

Emergent hadronic mass (EHM) is an elemental feature of the Standard Model. As reviewed elsewhere [4-6]: it is the origin of a running gluon mass; the source of dynamical chiral symmetry breaking (DCSB); and very probably crucial to any explanation of confinement. DCSB is basic to understanding the notion of constituent quarks and the successes of related models; and it provides the foundation for the existence of nearly-massless pseudo-Goldstone modes. Confinement is related to the empirical fact that all attempts to remove a single quark or gluon from within a hadron and isolate it in a detector have failed. The mechanisms responsible for EHM must be expressed, besides in hadron masses, in their wave functions with the associated Fock-space representation in terms of quarks and gluons; especially, in the corresponding light-hadron structure observables. In the following, examples of such measurable quantities will be presented, focused largely on pion and kaon observables accessible at EIC. The kaon is very interesting because therein a competition between emergent and Higgs-driven mass generation is taking place. All differences between the pion and kaon are driven by Higgs-induced modulation of EHM.

*2.1.1. Pion and kaon distribution amplitudes.* The cross sections for many hard exclusive hadronic reactions can be expressed in terms of the parton distribution amplitudes (DAs) of the hadrons involved. For instance, in the case of the



electromagnetic form factor of light pseudoscalar mesons [18–21]:

$$\exists Q_0 > \Lambda_{\text{QCD}} \mid Q^2 F_P(Q^2) \stackrel{Q^2 > Q_0^2}{\approx} 16\pi\alpha_s(Q^2) f_P^2 w_\varphi^2, \text{ with } w_\varphi = \frac{1}{3} \int_0^1 dx \frac{1}{x} \varphi_P(x), \quad (5)$$

where  $\alpha_s(Q^2)$  is the strong running coupling,  $f_P$  is the pseudoscalar meson’s leptonic decay constant and  $\varphi_P(x)$  is the DA of the pseudoscalar meson. However, the value of  $Q_0$  is not predicted by QCD and the DAs are not determined by the analysis framework; perturbative QCD (pQCD) only states that  $\varphi_P(x) \approx \varphi_{\text{as}}(x) = 6x(1-x)$  for  $Q^2 \gg Q_0^2$ .

One may alternatively use continuum Schwinger function methods (CSMs) for QCD to describe exclusive reactions in terms of Poincaré-covariant hadron bound-state amplitudes (BSAs). This approach has been formulated in both Euclidean [22–26] and Minkowski [27–32] space. Moreover, recent progress within CSMs has established that the hadron DA, which is essentially nonperturbative, can be obtained as a light-front projection of the hadron’s BSA [33], an approach first employed in [34]. Using this connection, the solid curves of figure 2 are the CSM’s predictions for the pion [35, 36] and kaon [37] elastic electromagnetic form factors to arbitrarily large- $Q^2$ . Also depicted (dashed curves) are the results obtained using equation (5) and the DAs calculated in the CSM framework at a scale relevant to the experiment. These DAs are very different from  $\varphi_{\text{as}}(x)$ , being markedly broader owing to EHM. The dotted curve in both panels is the hard scattering formula, equation (5), computed with the asymptotic profile,  $\varphi_{\text{as}}(x)$ .

EIC is capable of providing precise pion form factor data that will probe deep into the region where  $F_\pi(Q^2)$  exhibits strong sensitivity to EHM and the evolution of this effect with scale. In particular, as more results from Euclidean and Minkowski space approaches within the CSM framework become available, an estimate of a lower bound for  $Q_0$  can be found by comparing the full covariant form factor with the valence one, which should dominate at large momenta, with the difference quantifying the contribution from the higher Fock-components of the light-front wave function to the pion charge distribution. The extraction of the pion form factor via a Sullivan process involves the extrapolation to an off-mass-shell pion that can be quantified and validated [43, 44]. Moreover, the EIC will be the first facility to measure the size and range of nonperturbative EHM–Higgs-boson interference effects in hard exclusive processes if high- $Q^2$  kaon form factor measurements can be feasible at EIC.

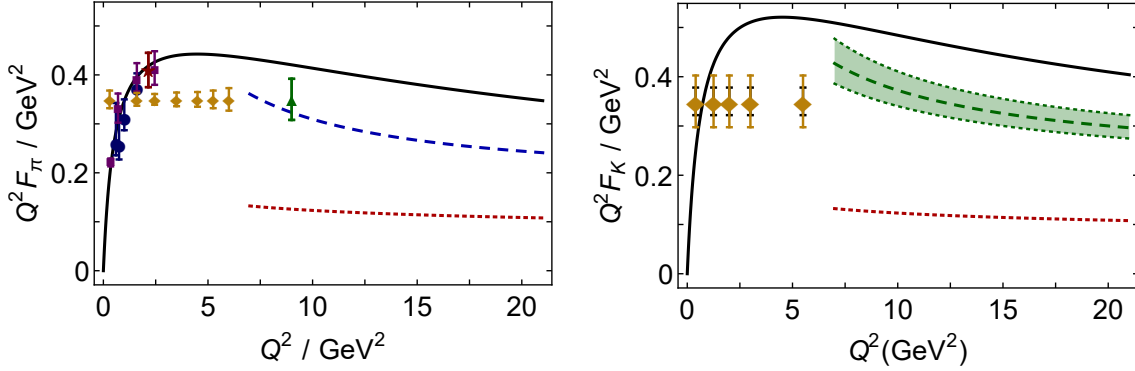


Figure 2: The left (right) panel show calculations, measurements, and projected precision of future measurements for  $Q^2 F_\pi(Q^2)$  ( $Q^2 F_K(Q^2)$ ). Solid curve – prediction from [35, 36]; dotted curve – result produced by the hard scattering formula, equation (5), using the asymptotic DA; dashed curve – result produced by the hard scattering formula using the DA calculated in the CSM framework at a scale relevant to the experiment. Stars [38], circles and squares [39] show existing data; diamonds and triangle show the anticipated reach and accuracy of forthcoming experiments [40–42].

*2.1.2. Pion and kaon distribution functions.* The pion valence quark distribution function (DF),  $q^\pi(x, \zeta)$ , expresses the probability density that a valence  $q$ -quark in the pion carries a light-front fraction  $x$  of the system’s total momentum at a resolving scale  $\zeta$  [45]. In this connection, capitalising on the known behaviour of hadron wave functions at large valence-quark relative momenta [21, 46–48], numerous analyses within a diverse array of frameworks predict the following large- $x$  behaviour (see e.g. [49–53]):

$$q_\pi(x; \zeta = \zeta_H) \stackrel{x \simeq 1}{\sim} (1-x)^\beta, \text{ with } \beta = 2, \quad (6)$$

where  $\zeta_H$  is the hadronic scale, which is not accessible in experiment because certain kinematic conditions must be met in order for the data to be interpreted in terms of  $q_\pi(x, \zeta)$  [45]. Hence, any result for a distribution function at  $\zeta_H$  must be evolved to  $\zeta_E (> \zeta_H)$  for comparison with experiment [54–57]. Under such evolution, the exponent grows, viz.  $\beta = 2 + \delta$ , where  $\delta$  is an anomalous dimension that increases logarithmically with  $\zeta$ . Significantly, within DF fitting uncertainties, the analogous behaviour for the proton’s valence-quark distribution function has been confirmed [58].

It is worth noting here that what has come to be known as the Drell-Yan-

West relation provides a link between the large- $x$  behaviour of DFs and the large- $Q^2$  dependence of hadron elastic form factors [59, 60]. In its original form, the relation was discussed for the  $J = 1/2$  proton. It has long been known that this original form is invalid when, e.g. the target is a ( $J = 0$ ) pseudoscalar meson and the valence-parton scatterers are  $J = 1/2$  objects [61, 62]. The generalisation to spin- $J$  targets constituted from  $J = 1/2$  quarks may be found in [52]: for a hadron  $H$  defined by  $n + 1$  valence  $J = 1/2$  partons, so that its leading elastic electromagnetic form factor scales as  $(1/Q^2)^n$ :

$$q_H(x; \zeta_H) \stackrel{x \approx 1}{\sim} (1-x)^p, p = 2n - 1 + 2\Delta S_z, \quad (7)$$

where  $\Delta S_z = |S_z^q - S_z^H|$ . For a pseudoscalar meson,  $n = 2$ ,  $S_z^H = 0$ , so  $p = 2$ . One thereby recovers Eq. (6).

Experiments interpretable in terms of  $q_\pi(x, \zeta)$  were completed more than thirty years ago [63, 64]. Notably, phenomenological analyses of that data which ignore soft-gluon (threshold) resummation effects return a DF that roughly resembles a profile with  $\beta \approx 1$  [65–67], in conflict with equation (6). On the other hand, [68], which included such next-to-leading-logarithm resummation using the “cosine method”, yields  $\beta > 2$ , in accord with equation (6). The dependence of the inferred large- $x$  behaviour of DFs on the resummation prescription is being explored [69]: preliminary findings suggest that, depending on the method adopted (“double Mellin”, “expansion” or “cosine”), the apparent  $\beta$  exponent can range between  $\sim 1$  and  $\sim 2.5$  at the input scale. Importantly, however, all methods yield softened large- $x$  behaviour, with both the *expansion* and *cosine* approaches producing  $\beta > 2$ . Additional remarks on these issues are presented in section 2.3.

The CSM prediction [70, 71] for  $u_\pi(x; \zeta_5)$  is depicted in the left panel of figure 3. Its large- $x$  behaviour agrees with equation (6) and the pointwise form matches that determined in [68]. Regarding glue and sea DFs, [70, 71] provide parameter-free predictions for all pion DFs.

Notably, as described in section 2.2, lattice-regularised QCD is now beginning to yield results for the pointwise behaviour of the pion’s valence-quark distribution [72, 73], with that delivered by the approach in [72] being in fair agreement with both equation (6) and the CSM prediction. This is highlighted by the comparison between the blue CSM result and the dot-dot-dashed (grey) curve in the left panel of figure 3.

Parameter-free predictions for all kaon DFs are also provided in [70, 71]. Concerning valence-quarks, there are qualitative similarities between  $u_K(x)$ ,  $\bar{s}_K(x)$

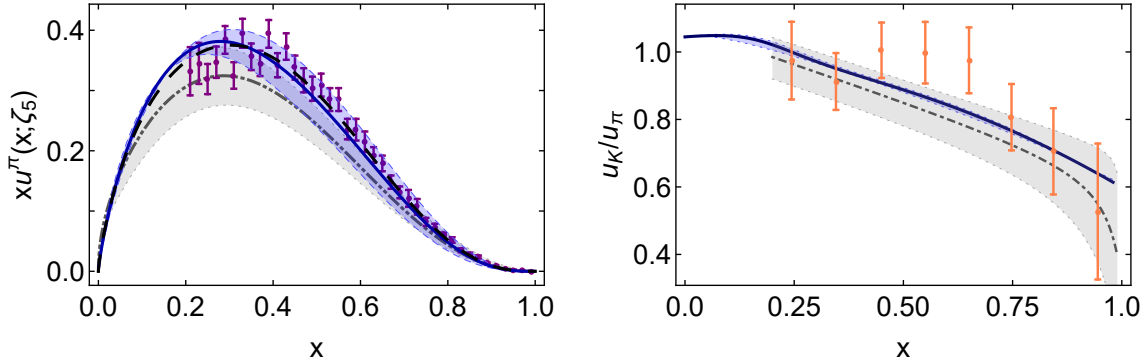


Figure 3: *Left panel.* Pion valence-quark momentum distribution function,  $xq_\pi(x; \zeta_5 = 5.2 \text{ GeV})$ : solid blue curve – modern continuum calculation [70, 71]; long-dashed black curve – early continuum analysis [74]; and dot-dot-dashed grey curve – lattice QCD result [72]. Data (purple) from [64], rescaled according to the analysis in [68]. *Right panel.*  $u_K(x; \zeta_5)/u_\pi(x; \zeta_5)$ . Solid blue curve – prediction from [70, 71]. Dot-dashed grey curve within grey band – lattice QCD result [75]. Data (orange) from [76].

and  $u_\pi(x)$ , e.g. all three DFs are consistent with equation (6) so that  $\bar{s}_K(x)$  is much softer than the lattice-QCD result drawn in figure 5–left. There are also quantitative differences between the valence distributions, as highlighted by the prediction for  $u_K(x)/u_\pi(x)$  drawn in figure 3–right and compared with the result determined from a measurement of the  $K^-/\pi^-$  structure function ratio [76].

The first lattice-QCD results for  $u_K(x)/u_\pi(x)$  are also drawn in figure 3–right. The relative difference between the central lattice QCD result and the continuum prediction [70, 71] is  $\approx 5\%$ , despite the fact that the individual DFs from these two sources are qualitatively and quantitatively different. This feature highlights a long known characteristic, i.e.  $u_K(x)/u_\pi(x)$  is quite forgiving of even large differences between the individual DFs used to produce the ratio. Evidently, more precise data is crucial if this ratio is to be used effectively to inform and test the modern understanding of pion and kaon structure; and results for  $u_\pi(x; \zeta_5)$ ,  $u_K(x; \zeta_5)$  separately have greater discriminating power. These remarks are amplified by the fact that the lone  $K^-/\pi^-$  structure function experiment was performed forty years ago. Hence, new precision data and extractions must be a high priority.

Significantly, [70, 71] also provides the first parameter-free predictions for the ratios

of glue and sea DFs in the pion and kaon. The kaon's glue and sea distributions are similar to those in the pion; but the inclusion of mass-dependent splitting functions, expressing Higgs-induced current-quark mass splittings, introduces differences on the valence-quark domain. Today, no empirical information is available that would enable these predictions to be tested. Hence, experiments sensitive to glue and sea distributions in the kaon and pion would be of enormous value.

Euclidean-space based CSMs obtain the pion's DFs considering it as a bound-state of a dressed-quark and dressed-antiquark at the hadronic scale, with the sea and glue distributions being zero at  $\zeta_H$  and generated by evolution on  $\zeta > \zeta_H$  [77, 78]. This is also the case for the kaon. In contrast, a Minkowski space analysis of the Bethe-Salpeter equation finds that the valence-quark probability in the pion state is about 70% [79] with the remaining normalisation distributed among higher Fock-space components, carrying gluons at the hadronic scale. A resolution of this puzzle will likely be found in the mapping between the different quasi-particle degrees-of-freedom that serve in each calculation.

Related analyses of pseudoscalar meson generalised transverse momentum dependent DFs (GTMDs) are also becoming available [80]. They indicate that GTMD size and shape are also prescribed by the scale of EHM. Proceeding from GTMDs to generalised parton distributions (GPDs) [80–85], it is found that the pion's mass distribution form factor is harder than its electromagnetic form factor, which is harder than the gravitational pressure distribution form factor; the pressure in the neighbourhood of the pion's core is similar to that at the centre of a neutron star; the shear pressure is maximal when confinement forces become dominant within the pion; and the spatial distribution of transversely polarised quarks within the pion is asymmetric.

Regarding transverse momentum dependent distribution functions (TMDs), these studies indicate that their magnitude and domain of support decrease with increasing twist [80]. Consistent with intuition [80], at  $\zeta_H$ , the simplest Wigner distribution associated with the pion's twist-two dressed-quark GTMD is sharply peaked on the kinematic domain associated with valence-quark dominance; has a domain of negative support; and broadens as the transverse position variable increases in size.

More sophisticated studies are beginning to appear. For instance, [85] computes and compares pion and kaon GPDs built using the overlap representation from light-front wave functions constrained by the one-dimensional valence distributions described above. It finds, *inter alia*, that  $K$  pressure profiles are spatially more compact than

$\pi$  profiles and near-core pressures in both NG modes are of similar magnitude to that found in neutron stars. Plainly, now is the right time to plan on exploiting the capacities of EIC to probe these higher-dimensional aspects of pion and kaon structure.

## 2.2. Pion and kaon Structure - lattice QCD status

Quantising QCD on a finite-volume discrete lattice in Euclidean space-time enables the numerical calculation of correlation functions defined by the functional integral [86]. Accessing hadron structure information using lattice QCD has been a very challenging task, since distribution functions are light-cone quantities and cannot be calculated directly on a Euclidean lattice. Over the years, a range of methods have been proposed to overcome this obstacle, such as studies based on the hadronic tensor [87–89], auxiliary quark field approaches [90, 91], large-momentum effective theory (LaMET) [92–94] (quasi-PDFs), pseudo-PDFs [95], an operator-product-expansion based method [96], and the good lattice cross sections (LCS) approach [97–99]. These methods have some common ground, but also differences. Interested readers may consult [94, 100, 101] for more details. This subsection describes a few examples of recent progress in meson structure studies and indicates calculations that will be important for the success of EIC science.

*2.2.1. Meson distribution amplitudes* The  $x$ -dependent quark distribution amplitudes (DAs) of the pseudoscalar mesons have been calculated both in the LaMET approach [73, 102] and using a current-current approach analogous to LCS [103, 104]. [102] studied the pion-mass dependence of the pion distribution amplitude on the lattice in the continuum limit as determined from three lattice spacings: 0.06, 0.09, 0.12 fm. Figure 4 shows pion DA results at pion masses of 690 MeV and 310 MeV, together with their extrapolation to 135 MeV. Note that the chiral extrapolation of [102] is dominated by the 310-MeV calculations. The lattice kaon DA is shown on the right-hand-side of figure 4. The kaon DA is narrower than that of the pion, as suggested in [6, 105]. The variation of the DA shapes with quark mass helps to understand the origin of mass [13].

*2.2.2. Meson parton distribution functions.* The advances in computing hadron structure from calculations on a Euclidean lattice are transforming our ability to study the DFs of mesons within lattice QCD. Many of the challenges in capitalising on these advances mirror those encountered in the global fitting community, most notably in

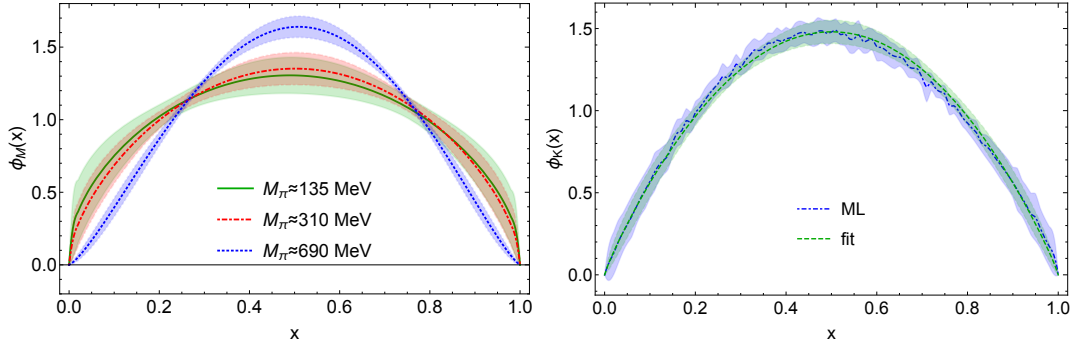


Figure 4: *Left panel.*  $x$ -dependent pion DA at two different pion masses, along with an extrapolation to the physical pion mass. As the pion mass decreases, the distribution amplitude become broader. The calculations use meson boosted momentum of  $P_z = 1.73 \text{ GeV}$  and are renormalised at  $2 \text{ GeV}$  in  $\overline{MS}$  scheme. *Right panel.*  $x$ -dependent kaon DA obtained using a fit to lattice results obtained through a machine-learning approach [102].

obtaining a faithful description of DFs from incomplete data; in the case of lattice calculations, the advent of exascale computing, the application of novel methods – such as Bayesian approaches, and machine learning promise to enable us to address and overcome these challenges.

*2.2.3. Valence quark distribution.* The valence quark distributions are the most widely studied distributions within lattice QCD and where these new approaches have shown the most immediate impact. Notably, calculations of the  $x$ -dependent DFs of the pion have been performed at close-to-physical light-quark masses, with increasing control over the systematic uncertainties arising from the finite-volume and discretisation systematic uncertainties. Calculations have been performed within the LaMET [73, 75, 106], pseudo-PDF [107] and LCS frameworks [72, 108]. Most recently, these methods have been applied to the valence quark distributions of the kaon [75], as illustrated in Fig. 5, and the  $u_K/u_\pi$  ratio, as discussed in connection with Fig. 3. These calculations are becoming comparable with extant data over a large range of  $x$ ; and arrival of the exascale era will enable them to be refined, especially with a view to determination of the large- $x$  behaviour of the PDFs, whose significance is discussed in connection with Eq. (6).



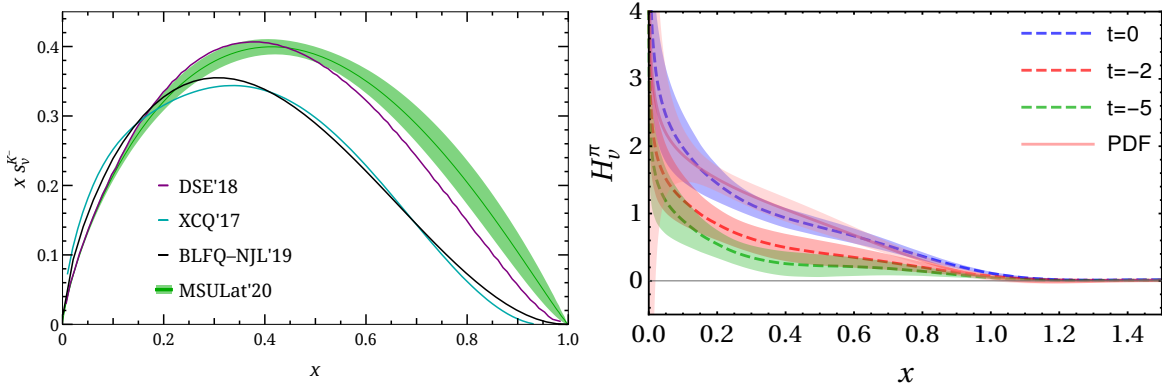


Figure 5: *Left panel.* Lattice results for  $x\bar{s}_v^K(x)$  as a function of  $x$  (labelled as “MSULat’20”) [75]. Some model studies are shown for comparison. Additional discussion may be found elsewhere [71, section 7.2]. *Right panel.* Lattice results for the zero-skewness pion valence quark GPD  $H_v^{\pi^+}(x, \xi = 0, t, \zeta = 4 \text{ GeV})$  for  $t = \{0, -2, -5\}(2\pi/L)^2$  after one-loop matching and meson-mass corrections [109]. “PDF” denotes the pion DF result in [73].

*2.2.4. Gluon distribution.* Within lattice QCD, gluonic and flavour-singlet quantities are much noisier than valence-quark distributions. Thus, a far larger statistical sample is required to reveal a signal. The first exploratory gluon DF study applied the quasi-PDF approach to the gluon DFs [110], using ensembles with unphysically heavy quark masses corresponding to pion masses 340 and 678 MeV. Unfortunately, the noise-to-signal ratio grows rapidly with the dimensionless parameter  $zP_z$  and only coordinate-space gluon quasi-PDF matrix element ratios results are presented. Since then, there have also been developments in improving the operators for the gluon DF lattice calculations [111–113], which should enable evaluation of the continuum limit in future lattice calculations of gluon DFs. The pseudo-PDF approach developed in [111], along with improved methods of calculation for reaching higher boosted momentum, have recently been used to provide the first result for the nucleon gluon DF [114]. The prospects for applications to the cases of the pion and kaon appear promising, so that one may anticipate the appearance of increasingly precise calculations over the next few years.



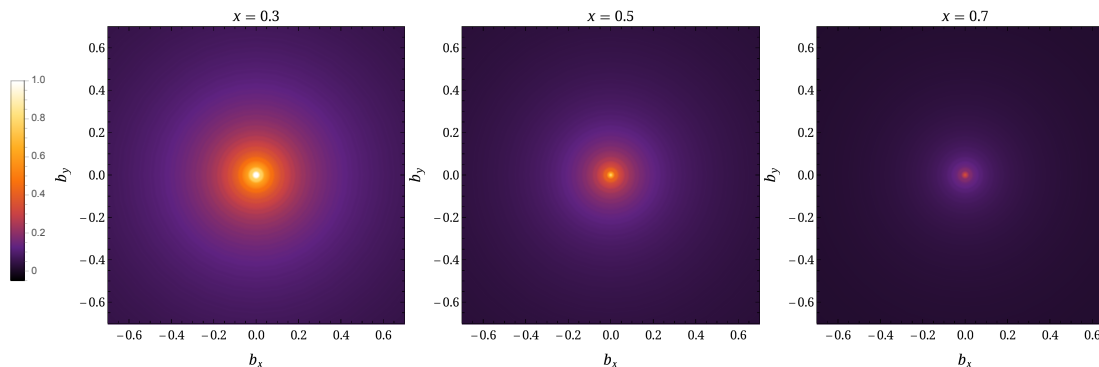


Figure 6: The two-dimensional impact-parameter-dependent distribution,  $\mathbf{q}(x, b)$ , for  $x = 0.3, 0.5$  and  $0.7$  determined from a lattice-QCD calculated pion GPD at physical pion mass.

*2.2.5. Pion GPDs.* In [109], the pion valence quark GPD at zero skewness was calculated using clover valence fermions on an ensemble of gauge configurations with  $2 + 1 + 1$  flavours (degenerate up/down, strange and charm) of highly-improved staggered quarks with lattice spacing  $a \approx 0.12$  fm, box size  $L \approx 3$  fm and pion mass  $m_\pi \approx 310$  MeV. The result is shown in figure 5–right. It turns out that, with current uncertainties, the result does not show a clear preference amongst different model assumptions about the kinematic dependence of the GPD. To distinguish between different models, further studies with higher-statistics will be crucial.

One may therefore anticipate that there will be lattice calculations of the pion’s valence quark GPD,  $H_\pi(x, \xi = 0, Q^2)$ , within the next few years. The Fourier transform of this GPD gives the impact-parameter-dependent distribution,  $\mathbf{q}(x, b)$  [115, 116]:

$$\mathbf{q}(x, b) = \int \frac{d\mathbf{q}}{(2\pi)^2} H_\pi(x, \xi = 0, t = -\mathbf{q}^2) e^{i\mathbf{q} \cdot \mathbf{b}}, \quad (8)$$

where  $b$  is the light-front distance from the transverse center of momentum (CoTM). Figure 6 shows the two-dimensional distributions at  $x = 0.3, 0.5, 0.7$ . The impact-parameter-dependent distribution describes the probability density for a parton with momentum fraction  $x$  to be found in the transverse plane at distance  $b$  from the CoTM. It provides a snapshot of the pion in the transverse plane and indicates what might be expected from nucleon tomography.

### 2.3. Global QCD analysis

Extracting information about DFs (or any partonic content of hadrons) from experimental data is a challenging problem in hadronic physics. Since the Lagrangian partons can never be isolated as free particles, details about their properties must be inferred indirectly by exploiting theoretical tools, such as QCD factorisation theorems [117]. The latter allow experimental observables in certain kinematic regions, *viz.*  $M_N^2/[(1-x)Q^2] \ll 1$ , to be written as convolutions of perturbatively-calculable hard scattering cross sections and nonperturbative DFs parametrising long-distance quark-gluon physics. The most robust method to extract information about DFs from experiment is through global QCD analyses of various QCD-factorisable hadronic processes that are sensitive to different combinations of DFs [65, 66, 69, 118–123].

Historically, the main experimental observables that have been used to constrain pion DFs have come from pion-nucleus collisions with inclusive production of lepton pairs or prompt photons [63, 124, 125]. More recently, leading neutron electroproduction data [126, 127] have been used to constrain pion DFs at small  $x$ , assuming the validity of pion exchange at small values of the transverse momentum and large longitudinal momentum of the produced neutron [126–128].

Important questions remain, however, concerning the fraction of the pion's momentum carried by gluons relative to the valence and sea quarks, and the behaviour of DFs at small and large values of  $x$ . For the latter, many calculations have been completed, with the exponent on  $(1-x)^\beta$  ranging from  $\beta \sim 0$  to  $\beta \sim 2$ . This was highlighted in [129] and in a raft of calculations since then, e.g. [70, 71, 77, 78, 80, 130–136]. In model calculations [80, 130–136], the energy scale and the value of  $x$  at which the asymptotic behaviour should be evident is *a priori* unknown. On the other hand, as noted in connection with Eq. (6), all calculations which enable a connection to be drawn between the underlying meson-binding dynamics and the valence-quark DF show that  $\beta$  is determined by the behaviour of the quark-antiquark interaction. Concerning data analyses, as already noted, inclusion and/or treatment of soft-gluon resummation can affect the inferred large- $x$  PDF behaviour [68, 69, 137–140], and the interplay of resummation and fixed-order calculations needs to be better understood.

The detailed  $x$  dependence of pion DFs is clearly a topic of considerable theoretical and phenomenological interest, and more data over a large range of kinematics would be helpful to unravel this structure. A programme of leading baryon production in inclusive deep inelastic scattering (DIS) from the deuteron with proton tagging

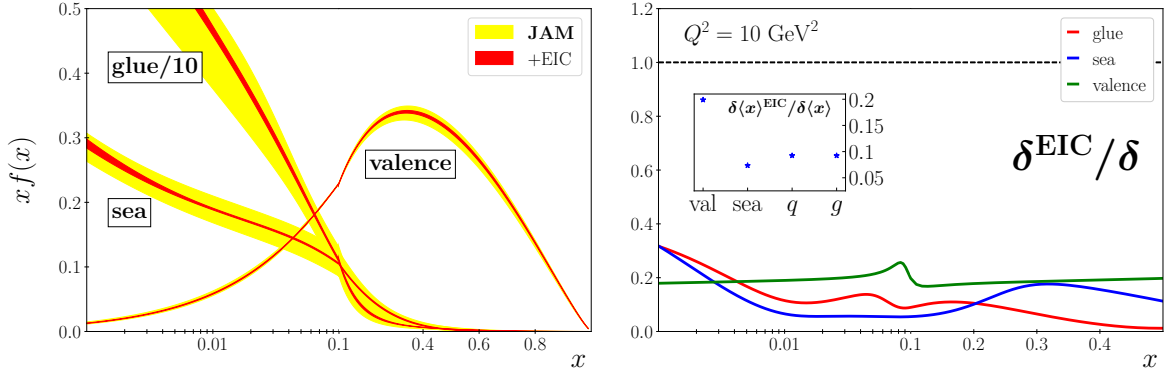


Figure 7: *Left panel.* Comparison of uncertainties on the pion’s valence, sea quark and gluon PDFs before (yellow bands) and after (red bands) inclusion of EIC data. *Right panel.* Ratio of uncertainties with EIC data to without,  $\delta^{\text{EIC}}/\delta$ , for the valence (green line), sea quark (blue) and gluon (red) PDFs, assuming 1.2% experimental systematic uncertainty but no model systematic uncertainty, and (inset) the corresponding ratios of the momentum fraction uncertainties,  $\delta\langle x \rangle^{\text{EIC}}/\delta\langle x \rangle$ , for valence, sea, total quark and gluon PDFs [69], at a scale  $Q^2 = 10 \text{ GeV}^2$ .

(“TDIS”) at Jefferson Lab [141] aims to explore the structure of pions emitted from the bound neutron [142], with generalisation to the hyperon case [143] aimed at investigating corresponding kaon structure observables. Complementing HERA and JLab measurements, EIC data on leading neutron and hyperon production can provide information on the role of the nucleon’s peripheral structure in a unique region interpolating between these kinematics. Especially in this interpolation region, EIC’s combination of high precision and wide kinematical coverage from  $Q^2 \sim [\text{few GeV}^2]$  to  $Q^2 \sim \mathcal{O}(100 \text{ GeV}^2)$  suggests a significant potential to constrain scaling violations in the pion structure function. This, in turn, may afford a higher level of discriminating power in unravelling the pion’s gluon content from the corresponding valence-/sea-quark contributions.

The potential impact of EIC neutron production data is illustrated in figure 7, which shows the valence, sea quark and gluon PDFs in the pion from the JAM global QCD analysis at the evolved scale  $Q^2 = 10 \text{ GeV}^2$  [65], comparing current uncertainties with those expected following the addition of EIC data [69]. The analysis of the existing data includes pion-nucleus Drell-Yan cross sections, both  $p_T$ -differential and

$p_T$ -integrated, and the leading neutron structure functions from HERA [144]. The analysis assumes a centre-of-mass (CM) energy  $\sqrt{s} = 73.5$  GeV for an integrated luminosity  $\mathcal{L} = 100 \text{ fm}^{-1}$  and a 1.2% systematic uncertainty across all kinematics. For both the sea quark and gluon distributions, the PDF uncertainties reduce by a factor  $\sim 5$ –10 for most of the  $x$  range, with a similar factor  $\sim 5$  reduction in the valence sector. For a decomposition of the pion mass written in terms of QCD stress-energy tensor matrix elements [145], the first moments,  $\langle x \rangle_{q,g}$ , are relevant. However, as discussed in connection with Fig. 1, the meaning of such a frame and scale dependent decomposition is uncertain [4, section V], [5, sections 4.4, 4.5]. Notwithstanding that, such moments are interesting in themselves, so it is worth noting that the reduction in associated uncertainties is a factor  $\approx 10$  for both the total quark and gluon contributions, as can be seen in the inset of figure 7–right. Note, however, that the errors do not include uncertainties associated with the model dependence of the “pion flux,” which may be of the order 10% – 20% [126, 127], and might reduce the impact of the projected data on the pion PDF uncertainties. A similar analysis may be performed for the PDFs in the kaon, which can be obtained from leading hyperon production in the forward region. In this case, the near-absence of empirical information on the parton structure of kaons will mean an even more striking impact of new EIC data.

For the impact study of the pion PDFs the uncertainties on the differential cross section were used. These are shown in figure 8 as a function of  $x_\pi$  and further discussed in section 5.1. The systematic uncertainty is 1.2% (magenta squares); the statistical uncertainties are on average less than 0.5% and vary as a function of  $x_\pi$  and  $Q^2$  (filled circles). The statistical uncertainty is smallest at small  $x_\pi$  and  $Q^2$  and increases with increasing values of  $x_\pi$  and  $Q^2$ . Clearly for much of the range  $x_\pi \lesssim 0.8$ , the systematic uncertainties dominate the statistical uncertainties. This was not the case with the same observable in the HERA experiments [126, 127]. Because the integrated luminosity for the EIC is projected to be about three orders of magnitude greater than that for HERA, the total uncertainty quantification will be largely driven by the systematic uncertainties.

#### 2.4. Synergy between theory calculations and data analysis

In comparison with the nucleon, experimental probes of the pion and kaon have been relatively sparse, with substantial ambiguities remaining regarding their partonic, quark-gluon substructure. Partly for this reason, one may expect future knowledge

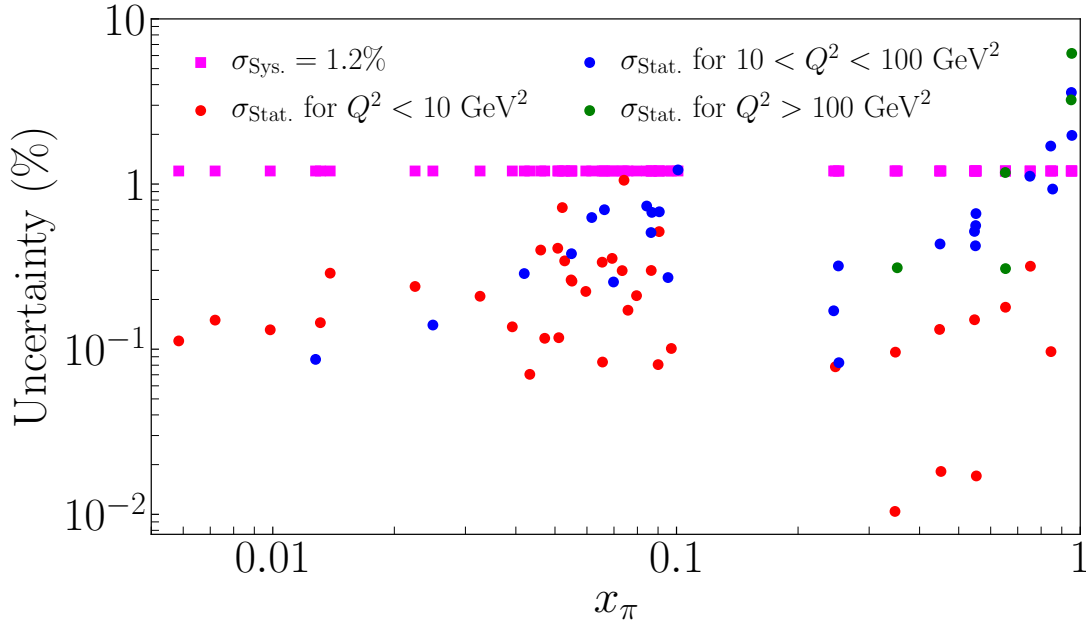


Figure 8: Fractional uncertainties of the cross section projected data as used for the pion PDF impact analysis in figure 7. The statistical uncertainties  $\sigma_{\text{Stat.}}$  are shown as circles, separated in color by the ranges in  $Q^2$ . The assumed systematic uncertainty  $\sigma_{\text{Sys.}}$  of 1.2% are shown in the magenta squares.

of the pion to derive from an interplay among several methods (see Fig. 9): QCD phenomenology, including QCD-inspired models and continuum methods in Euclidean and Minkowski spaces; recent developments from lattice QCD; and QCD global analyses of both contemporary and future data. For the latter, EIC can be expected to furnish a significant amount of valuable data; and therefore to be a crucial driver of global theory efforts. Naturally, in the context of this discussion, the focus here is on the structure of NG modes as quantified via collinear parton distribution functions (PDFs), or, in the case of three-dimensional structure, GPDs and TMDs.

To explore possible synergies among the approaches sketched above, a number of theoretical issues require further development and understanding. The following are especially prominent.

- **Direct lattice calculation of distributions.** A major advance in the ability

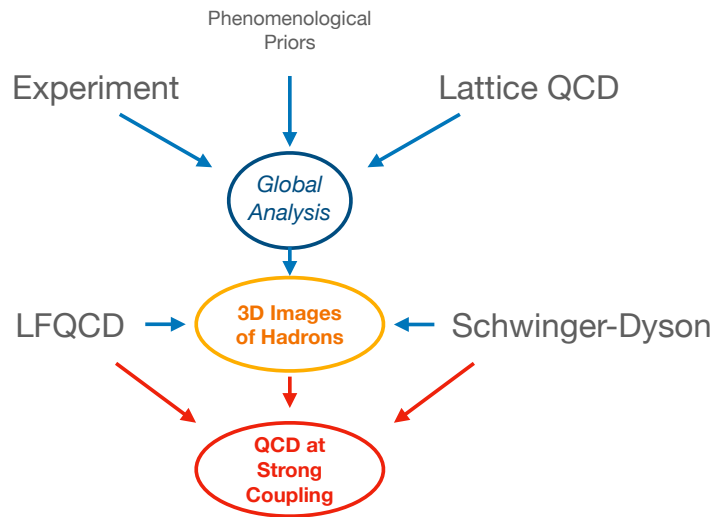


Figure 9: Potential interplay between QCD phenomenology, continuum approaches to QCD, lattice, global analysis and experiment.

to study the internal structure of hadrons from lattice QCD computations was the realisation that PDFs, and their three-dimensional extensions, described as matrix elements of operators separated along the light cone, could be related to quantities calculable in Euclidean space [92, 93, 99, 146]. Such calculations yield not pointwise evaluation of the PDFs at each Bjorken- $x$ , but rather convolutions of those PDFs with some calculable kernel, together with modifications in the manner of higher-twist and mass corrections. The resulting convolutions in practical lattice calculations yield functions that are incomplete and limited by the finite volume and discretisation of the lattice. The extraction of the  $x$ -dependent PDFs from such calculations therefore requires that an inverse problem be addressed, whose solution requires additional information.

The situation somewhat mirrors that of global fits to experimental data, when the desired PDFs generally arise, as in Drell-Yan processes, from a convolution with a perturbatively calculated kernel. For the case of one-dimensional distributions, such as PDFs, the additional information can be provided through an assumed PDF parametrisation so that extraction of the PDF becomes a parameter fitting exercise. That method has been central to the strategy of the global fitting

community and has likewise been adopted by several lattice collaborations. More recently, there has been an effort to incorporate different schemes, such as machine learning and Bayesian reconstruction [147, 148].

- **Inclusion of lattice results as data in QCD global analyses.** An evolving opportunity is to introduce results from lattice computations into the global fits [149], either in the same manner as experimental data, in the case of the nucleon PDFs [150], or as a Bayesian prior in the fit to experimental data, as was accomplished for the nucleon tensor charge [151]. The aim, at least for the nucleon, is not to test QCD, but rather to use both experiment and lattice computations to provide more information about key measures of hadron structure than either can alone. For pions and kaons, for which there are no free meson targets and structure is probed indirectly through the Sullivan process at EIC, lattice computations of the PDFs of a lone, isolated pion or kaon may assist in validating the experimental analysis, potentially providing benchmarks to quantify the effects of off-shellness or kinematical extrapolations in  $t$ ;

Lattice computation and experiment may also provide complementary information on hadron structure. Thus an important effort is the computation of gluon and flavour-singlet contributions to hadron structure, and those computations may predict the outcomes of experiment. Similarly, recent developments have enabled the calculation of the  $x$ -dependent GPDs, both for the nucleon [152, 153] and the pion [109] – see Fig. 5 – right, and the frameworks allow these distributions to be extracted at definite non-zero skewness [152, 154].

- **Benchmarking calculations with QCD fits and phenomenology.** PDF (or GPD/TMD) phenomenology can offer benchmarks for use in developing lattice and/or continuum QCD computations; in particular, the NNLO precision of contemporary *nucleon* PDF analyses in the unpolarised sector is such that these extractions can play an important role in testing analogous calculations of lattice quantities, such as PDF Mellin moments [155]. Similar arguments apply to recent QCD global analyses of meson structure noted above.
- **Relating Euclidean lattice QCD and continuum methods.** A number of formal developments related to treatments of the pion using CSMs, including Dyson-Schwinger equations and light-front quantisation, would also be helpful. Lattice studies long ago confirmed the continuum predictions of nonperturbative infrared dressing of gluons and quarks, which are the effective degrees-of-freedom

in the pion/kaon exploited by continuum methods. The light-front projection of a hadron's Bethe-Salpeter amplitude [27, 33] is linked to a Fock component in a basis whose character is specified by the resolving scale [71, section 2]. This projection is a gauge invariant probability density [156]. The hadron image on the null-plane [157], expressed by Ioffe time and transverse coordinates of dressed constituents, may be accessible along this path [158, 159];

- **Mapping the pion light-front wave function.** Understanding QCD on the null-plane will place the concept of the light-front wave function on firmer ground, allowing access to pion PDFs, GPDs, TMDs, and more [160] within a unified, invariant representation of the meson. A clear identification of the unitary transformation from the free light-front Fock-space basis to the one that entails dressed and confined constituents is necessary. To this end, investigations on the non-triviality of the vacuum and the role zero-modes in the light-front quantisation are on-going (see e.g. [161–165]).

It is worth reiterating that data supplied by EIC will provide a firm basis for new insights into pion and kaon structure. By significantly expanding the world's pool of data sensitive to light-meson structure functions, EIC will provide a setting to explore and refine the synergies enumerated above and sketched in figure 9. These refinements will occur along several tracks, providing new constraints to QCD fits of meson parton distributions, which will then be used to inform and validate continuum analyses in QCD and phenomenological calculations while also benchmarking rapidly-developing lattice efforts. These in turn can be expected to serve reciprocally as guidance for and constraints on QCD fits of data, including the highly anticipated EIC measurements envisioned in this work.

### 3. Key EIC measurements

It is here necessary to summarise the experimental requirements for critical EIC measurements that tackle some outstanding questions in the study of pion and kaon mass and structure. This will lead subsequently to an explanation of how these meson structure measurements, which serve as a laboratory in which fundamental aspects of QCD can be elucidated, complement and strengthen ongoing and foreseen programmes worldwide.

To facilitate this discussion, it is useful to translate current theory understanding of



light meson structure and emergent hadron mass (and structure) mechanisms into a set of critical science questions. Currently, not all these science questions are rigorously defined theoretically; but they do reflect the current state of understanding. These questions come from community discussions at a series of dedicated pion/kaon structure workshops (2017, 2018, 2019, and 2020), and at meetings related to the ongoing EIC Yellow Report activities. They represent outstanding mysteries that require further experimental (and theoretical) examination, and illustrate the impact of a coherent study of pion and kaon structure yielding results similar to present studies of proton structure.

Table 1 on page 29 lists the key science questions along with specific measurements required to advance community understanding. It also presents the high-level experimental needs, providing the minimum experimental requirements as well as improvements that could further expand these studies. Later sections will examine other important considerations aimed at demonstrating that one can extract pion and kaon structure information independent of the phenomenology ansatz, independent of physics background contributions, and independent of Mandelstam- $t$ . Some interesting science questions that may be more challenging to address are listed at the bottom of the table; they are considered more speculative because validating the reaction mechanism will be more challenging than the other cases, owing to considerations such as competing reaction and background mechanisms.

For all observables, a luminosity well above  $10^{33}$  is required to compensate for the (few times)  $10^{-3}$  fraction of the proton wave function related to the pion (kaon) Sullivan process. Also, a large range in  $x_L$  (the longitudinal energy fraction carried by the produced particle) is required, up to  $x_L \sim 1$  for  $ep$  reactions and  $x_L$  at least  $\sim 0.5$  for  $ed$  reactions. Data on negatively-charged pions (e.g.  $e+d \rightarrow e'+p+p+X$ ) and on neutral-pion channels (e.g.  $e+p \rightarrow e'+p+X$ ) are crucial to constrain reaction mechanisms and theory backgrounds in extracting the physical pion (kaon) target information.

### 3.1. Sullivan process

In specific kinematic regions, the observation of recoil nucleons (N) or hyperons (Y) in the semi-inclusive reaction  $ep \rightarrow e'(N \text{ or } Y)X$  can reveal features associated with correlated quark-antiquark pairs in the nucleon, referred to as the “meson cloud” of the nucleon. At low values of  $|t|$ , the four-momentum transfer from the initial proton to the final nucleon or hyperon, the cross section displays behaviour characteristic of

meson pole dominance. The reaction in which the electron scatters off the meson cloud of a nucleon target is called the Sullivan process [166]. For elastic scattering ( $X = \pi^+$  or  $K^+$ ), this process carries information on the pion or kaon form factor, and could be tagged by detection of a recoil nucleon or hyperon, respectively. For DIS, the typical interpretation is that the nucleon parton distributions contain a mesonic parton content. To access pion or kaon partonic content via such a structure function measurement requires scattering from a meson target, which again could be facilitated in the Sullivan process by detection of a recoil nucleon or hyperon.

The Sullivan process can provide reliable access to a meson target in the space-like  $t$  region, if the pole associated with the ground-state meson remains the dominant feature of the process and the structure of the related correlation evolves slowly and smoothly with virtuality. To check whether these conditions are satisfied empirically, one can take data covering a range in  $t$ , particularly low  $|t|$ , and compare with phenomenological and theoretical expectations. A recent calculation [43] explored the circumstances under which these conditions should be satisfied. For the pion (kaon) Sullivan process, low  $-t$  equates to  $-t < 0.6$  (0.9)  $\text{GeV}^2$  to be able to cleanly extract pion (kaon) structure, and data over a range of  $-t$  down to the lowest accessible are needed to verify pion (kaon) structure extraction.

### 3.2. Theoretical backgrounds in extracting the data

Extraction of the mesonic structure of the nucleon from the tagged DIS cross section is inherently model dependent. It will, therefore, be necessary to examine all reasonable models that are available (such as Regge models of baryon production and Dyson-Schwinger equation inspired models), or that may be available in the future, to evaluate the theoretical uncertainty associated with extracting meson structure functions from the tagged deep inelastic data. To clarify this model dependence, one can formally write, e.g. the measured semi-inclusive structure function of the leading proton,  $F_2^{LP(4)}$ , related to the measured cross-section as:

$$\frac{d^4\sigma(ep \rightarrow e' X p')}{dx dQ^2 dy dt} = \frac{4\pi\alpha^2}{xQ^4} \left[ 1 - y + \frac{y^2}{2(1+R)} \right] F_2^{LP(4)}(x, Q^2, y, t), \quad (9)$$

$y = P \cdot q / P \cdot l$ , where  $P(P')$  are the initial (scattered) proton four-vectors,  $l(l')$  are the initial (scattered) lepton vectors, and  $R$  is the ratio of the cross section for longitudinally and transversely polarised virtual photons. The measured cross section

can be integrated over the proton momentum (which is effectively an integration over  $t$  [167]) to obtain the leading proton structure function  $F_2^{LP(3)}$ . The pion structure function  $F_2^\pi$  can then be extracted from  $F_2^{LP(3)}$  using models, such as the Regge model of baryon production. In the Regge model, the contribution of a specific exchange  $i$  is defined by the product of its flux  $f_i(y, t)$  and its structure function  $F_2^i$  evaluated at  $(x_i, Q^2)$ . Thus,

$$F_2^{LP(3)} = \sum_i \left[ \int_{t_0}^{t_{\min}} f_i(z, t) dt \right] F_2^i(x_i, Q^2), \quad (10)$$

where  $i$  is the pion,  $\rho$ -meson etc, and the  $t$  corresponds to the range of  $p_T$  analyzed.

Neglecting uncertainties in the evaluation of  $R = \sigma_L/\sigma_T$ , which should be a small quantity, the extraction of the pion structure function will have to be corrected for a number of complications to the simple Sullivan picture. These include non-pion pole contributions,  $\Delta$  and other  $N^*$  resonances, absorptive effects, and uncertainties in the pion flux. For example, the cross section for leading charged pion production from the neutron is about twice reduced by absorptive corrections from other mesons. While these corrections can be large and one cannot extract the pion structure function without their inclusion, detailed calculations do exist [168]. Moreover, these corrections are minimised by measuring at the lowest  $-t$  or tagged nucleon momentum possible from the reaction. This minimises the absorptive correction since, at lower momenta, the pion cloud is further from the bare nucleon. In addition, the low momentum ensures that the higher meson mass exchanges are suppressed by the energy denominator. Also, the charged pion exchange process has the advantage of less background from Pomeron and Reggeon processes [169], and the charged pion cloud is expected to be roughly double the neutral pion cloud in the proton.

Having data from *both* protons and deuterons will provide essential cross-checks for the models used in the extraction of the pion structure function. In the Regge model it is assumed that the neutral pion, the Pomeron and the  $f_2$  will be the leading contributions to the cross section from the proton while the charged pion,  $\rho$  and  $a_2$  are the leading contributions from the neutron [170, 171]. However, Regge phenomenology also predicts that the flux of Reggeons with isospin one ( $\rho$  and  $a_2$ ) account for only  $\approx 3\%$  of the flux of Reggeons with isospin zero ( $\omega$  and  $f_2$ ) [170]. It also predicts that, for the neutron, the contributions from charged pion exchange are an order of magnitude larger than the contributions from the  $\rho$  and  $a_2$  [168]. Pomeron exchange does not give a significant contribution since diffractive dissociation is believed to be

$\approx 6\%$  of the pion exchange contribution [168].

The measured tagged cross sections and extracted tagged structure functions can be analyzed within a Regge framework where, assuming the dominance of a single Regge exchange, the differential cross section for recoil baryon production as a function of  $z$  at fixed  $t$  should be proportional to  $z - n$ , where  $n = 2\alpha(t) - 1$ , and  $\alpha(t)$  specifies the Regge trajectory of the dominant exchange. For pion exchange, the  $n$  averaged over the  $t$  dependence is expected to be  $n \approx -1$ , while other Reggeons are expected to have  $n > -1$ . Thus, by comparing the  $z$  dependence of the cross sections from proton and neutron (deuteron) scattering, it should be possible to determine the dominant exchange mechanism(s). Further, if the predictions for pion exchange are found to describe the data, the pion flux from the Regge model fits to hadron-hadron data may be safely used to extract the pion structure function.

The largest uncertainty in extracting the pion structure function, however, will likely arise from the (lack of) knowledge of the pion flux in the framework of the pion cloud model. One of the main issues is whether to use the  $\pi NN$  form factor or the Reggeised form factor. The difference between these two methods can be as much as 20% [172]. From the  $N-N$  data the  $\pi NN$  coupling constant is known to 5% [173]. If we assume that all corrections can be performed with a 50% uncertainty, and we assume a 20% uncertainty in the pion flux factor, the overall theoretical, systematic uncertainty could approach 25%. The superior approach is to have a direct measurement of the pion flux factor by comparing with pionic Drell-Yan data. For example the pion structure function at  $x = 0.5$  has been measured using pionic Drell-Yan data to an accuracy of 5% (see, e.g. [125, 174]). New data from COMPASS should enable this possibility to be leveraged further and likely reduce projected uncertainties even more.

Science Question	Key Measurement[1]	Key Requirements[2]
What are the quark and gluon energy contributions to the pion mass?	Pion structure function data over a range of $x$ and $Q^2$ .	<ul style="list-style-type: none"> <li>Need to uniquely determine <math>e + p \rightarrow e' + X + n</math> (low -t)</li> <li>CM energy range <math>\sim 10</math>-100 GeV</li> <li>Charged- and neutral currents desirable</li> </ul>
Is the pion full or empty of gluons as viewed at large $Q^2$ ?	Pion structure function data at large $Q^2$ .	<ul style="list-style-type: none"> <li>CM energy <math>\sim 100</math> GeV</li> <li>Inclusive and open-charm detection</li> </ul>
What are the quark and gluon energy contributions to the kaon mass?	Kaon structure function data over a range of $x$ and $Q^2$ .	<ul style="list-style-type: none"> <li>Need to uniquely determine <math>\Lambda, \Sigma^0</math>: <math>e + p \rightarrow e' + X + \Lambda/\Sigma^0</math> (low -t)</li> <li>CM energy range <math>\sim 10</math>-100 GeV</li> </ul>
Are there more or less gluons in kaons than in pions as viewed at large $Q^2$ ?	Kaon structure function data at large $Q^2$ .	<ul style="list-style-type: none"> <li>CM energy <math>\sim 100</math> GeV</li> <li>Inclusive and open-charm detection</li> </ul>
Can we get quantitative guidance on the emergent pion mass mechanism?	Pion form factor data for $Q^2 = 10$ -40 (GeV/c) $^2$ .	<ul style="list-style-type: none"> <li>Need to uniquely determine exclusive process <math>e + p \rightarrow e' + \pi^+ + n</math> (low -t)</li> <li>e-p and e-d at similar energies</li> <li>CM energy <math>\sim 10</math>-75 GeV</li> </ul>
What is the size and range of interference between emergent-mass and the Higgs-mass mechanism?	Kaon form factor data for $Q^2 = 10$ -20 (GeV/c) $^2$ .	<ul style="list-style-type: none"> <li>Need to uniquely determine exclusive process <math>e + p \rightarrow e' + K^+ + \Lambda</math> (low -t)</li> <li>L/T separation at CM energy <math>\sim 10</math>-20 GeV</li> <li>e-p <math>\Lambda/\Sigma^0</math> ratios at CM energy <math>\sim 10</math>-50 GeV</li> </ul>
What is the difference between the impacts of emergent- and Higgs-mass mechanisms on light-quark behaviour?	Behaviour of (valence) up quarks in pion and kaon at large $x$	<ul style="list-style-type: none"> <li>CM energy <math>\sim 20</math> GeV (lowest CM energy to access large-x region)</li> <li>Higher CM energy for range in <math>Q^2</math> desirable</li> </ul>
What is the relationship between dynamically chiral symmetry breaking and confinement?	Transverse-momentum dependent Fragmentation Functions of quarks into pions and kaons	<ul style="list-style-type: none"> <li>Collider kinematics desirable (as compared to fixed-target kinematics)</li> <li>CM energy range <math>\sim 20</math>-140 GeV</li> </ul>
<b>More speculative observables</b>		
What is the trace anomaly contribution to the pion mass?	Elastic $J/\psi$ production at low $W$ off the pion.	<ul style="list-style-type: none"> <li>Need to uniquely determine exclusive process <math>e + p \rightarrow e' + \pi^+ + J/\psi + n</math> (low -t)</li> <li>High luminosity (<math>10^{34+}</math>)</li> <li>CM energy <math>\sim 70</math> GeV</li> </ul>
Can we obtain tomographic snapshots of the pion in the transverse plane? What is the pressure distribution in a pion?	Measurement of DVCS off pion target as defined with Sullivan process	<ul style="list-style-type: none"> <li>Need to uniquely determine exclusive process <math>e + p \rightarrow e' + \pi^+ + \gamma + n</math> (low -t)</li> <li>High luminosity (<math>10^{34+}</math>)</li> <li>CM energy <math>\sim 10</math>-100 GeV</li> </ul>
Are transverse momentum distributions universal in pions and protons?	Hadron multiplicities in SIDIS off a pion target as defined with Sullivan process	<ul style="list-style-type: none"> <li>Need to uniquely determine scattered off pion: <math>e + p \rightarrow e + h + X + n</math> (low -t)</li> <li>High luminosity (<math>10^{34+}</math>)</li> <li>e-p and e-d at similar energies desirable</li> <li>CM energy <math>\sim 10</math>-100 GeV</li> </ul>

Table 1: Science questions related to pion and kaon structure and understanding of the emergent-hadron mass mechanism possible accessible at an EIC, with the key measurement and some key requirements. Further requirements are addressed in the text.

### 3.3. Kinematics of interest to address specific theory questions

The science questions of interest summarised in table 1 require a range of physics processes, spanning from (tagged) inclusive structure function measurements to (tagged) exclusive measurements such as required for a form factor determination or meson femtography. In general, a large range of CM energies is required to access a wide range in  $x$  and  $Q^2$ , as relevant for pion (kaon) structure function measurements or hadron multiplicity measurements for a TMD programme. This has to be balanced against the requirement to uniquely determine the remnant nucleon (or  $\Lambda$  or  $\Sigma^0$ ) to ensure the scattering process occurs off a pion (kaon). The latter favours not-too-high CM energies to be able to uniquely determine the remnant  $\Lambda$  (or  $\Sigma^0$ ), both for missing-mass determination and to ensure their decays occur before detection. In addition, there is need for both  $ep$  and  $ed$  measurements at similar CM energies to validate the reaction mechanism and understanding. This drives the “typical” CM energy range for pion and kaon structure function measurements to  $\sim 10-100$  GeV. Higher CM energies will increase the range in  $Q^2$ . On the other hand, lower CM energies are preferable for accessing the large- $x$  region to determine the behaviour of the valence quarks in pions (or kaons). In this case, the figure of merit, folding in all kinematic effects, is optimised at the lowest CM energy that provides a sufficiently large  $Q^2$  for a clean interpretation of the data.

For pion (kaon) fragmentation processes, the collider kinematics greatly facilitate transverse-momentum dependent measurements at low scales ( $p_T < 1\text{GeV}$ ), and the largest range in CM energy is required. For some processes the exact CM energy is not that important, so long as one obtains sufficient phase space for particle electroproduction to boost the experimental cross section. For instance, this is true for the (deep) exclusive  $J/\Psi$  measurements to possibly constrain the QCD trace anomaly, and also for access to charged-current cross sections.

For pion (kaon) form factor determination, the situation is different. The standard method relies on Rosenbluth L/T-separated cross sections as the longitudinal (L) cross section enhances pion (kaon) pole sensitivity. Such measurements are best done at a relatively low CM energy range ( $\sim 10-20$  GeV). An alternate method to extract the pion form factor makes use of direct comparison of charged-pion cross sections for  $ep$  and  $ed$ . This method may be applicable up to higher CM energies (and higher  $Q^2$  values). Similarly, for the kaon form factor it may be possible to increase the  $Q^2$  range (as compared to that from L/T-separated cross sections) from the  $\Lambda/\Sigma^0$  cross

section ratios. The latter requires further study, but is only possible at CM energies,  $\sim 10 - 50$  GeV, where the  $\Lambda$  and  $\Sigma^0$  may be cleanly isolated.

#### 3.4. Complementarity with other facilities

The broad science programme to understand pion and kaon structure and the QCD mechanism behind the emergent hadron masses requires a strong interplay between experiment and theory, matching experimental prospects by new theoretical insights, rapid computational advances, and high-level QCD phenomenology. The EIC will play a key role in the experimental programme to chart in-pion and in-kaon distributions of, *inter alia*, mass, charge, magnetisation and angular momentum. Nonetheless, to provide experimental measurements guiding theoretical understanding requires a coherent, worldwide effort.

The unique role of EIC is its access to pion and kaon structure over a wide range of large CM energies:  $\sim 20 - 140$  GeV. Jefferson Lab will provide, at its CM energy  $\sim 5$  GeV, tantalising data for the pion (kaon) form factor up to  $Q^2 \sim 10(5)$  GeV<sup>2</sup>, and measurements of the pion (kaon) structure functions at large- $x$  ( $> 0.5$ ) through the Sullivan process.

AMBER will play a crucial role as they can uniquely provide pion (kaon) Drell-Yan measurements in the CM energy region  $\sim 10 - 20$  GeV [175]. Some older pion and kaon Drell-Yan measurements exist, but for the kaon this is limited to less than 10 data points worldwide, so these measurements are essential for a global effort aimed at pion structure function measurements (also providing a handle on determination of the so-called ‘‘pion flux’’ for EIC Sullivan process measurements) and a *sine qua non* for any kaon structure function data map. The AMBER data in themselves will already give new fundamental insights into the emergent hadron mass mechanism.

An Electron-Ion Collider in China (EicC) is under consideration with a similar CM energy range as AMBER ( $\sim 10 - 20$  GeV) and bridging the energy range from Jefferson Lab to EIC [176]. EicC on its own, and even more in combination with AMBER, can provide good access to the region  $x \gtrsim 0.01$  for pion, and especially kaon, structure function determination and the impact on emergent hadron mass mechanisms on valence quark and gluon structure. In addition, EicC can extend the Rosenbluth L/T-separated cross section technique beyond Jefferson Lab and access pion and kaon form factors to higher  $Q^2$  values, perhaps by a factor of 2 – 4.

The EIC, with its larger CM energy range, will clearly have the final word on the

contributions of gluons in pions and kaons as compared to protons. It will finally settle questions relating to the gluon content of Nature's NG modes when they are viewed with very high resolution, and vastly extend the  $(x, Q^2)$  range of pion and kaon charts and meson structure knowledge.

#### 4. Kinematic coverage and detector requirements

##### 4.1. Far-forward area setup.

The far-forward EIC detector is described in detail in the EIC Yellow Report [177]. Figure 10 shows the main elements of this far-forward region. For the detection of particles of relevance to meson structure studies, all sub-components of the far-forward area play an important role: detection in the B0 area, detection of decay products with off-momentum detectors, and detection of forward-going protons and neutrons with the Roman Pots and the Zero-Degree Calorimeter (ZDC).

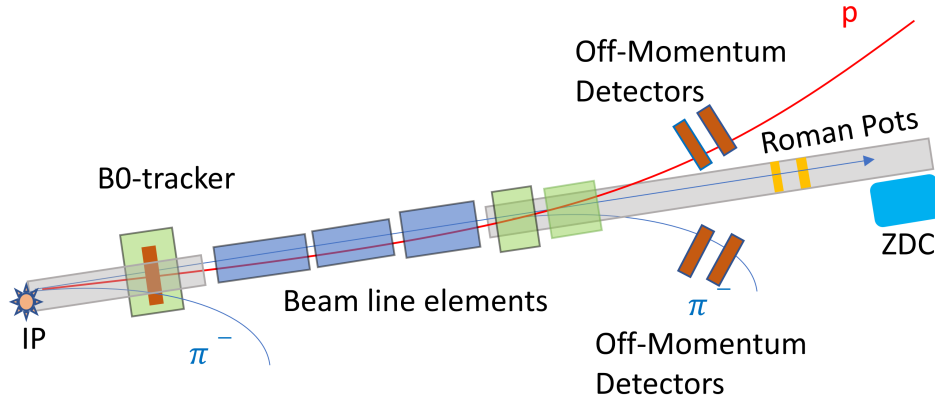


Figure 10: A sketch of the integrated beam line and detector setup in the Far-Forward area, along the direction of the proton/ion beam. The sketch is not to scale. The initial B0-tracker is integrated in the warm area of a combined electron-proton/ion beam magnet. Then a set of beam line magnetic elements follows that is integrated in one cryostat. This is followed by off-momentum detectors that capture the charged-particle decay products, roman pots that capture far-forward going protons with nearly the energy of the proton/ion beams, and the Zero-Degree Calorimeter to capture far-forward-going neutral particles.



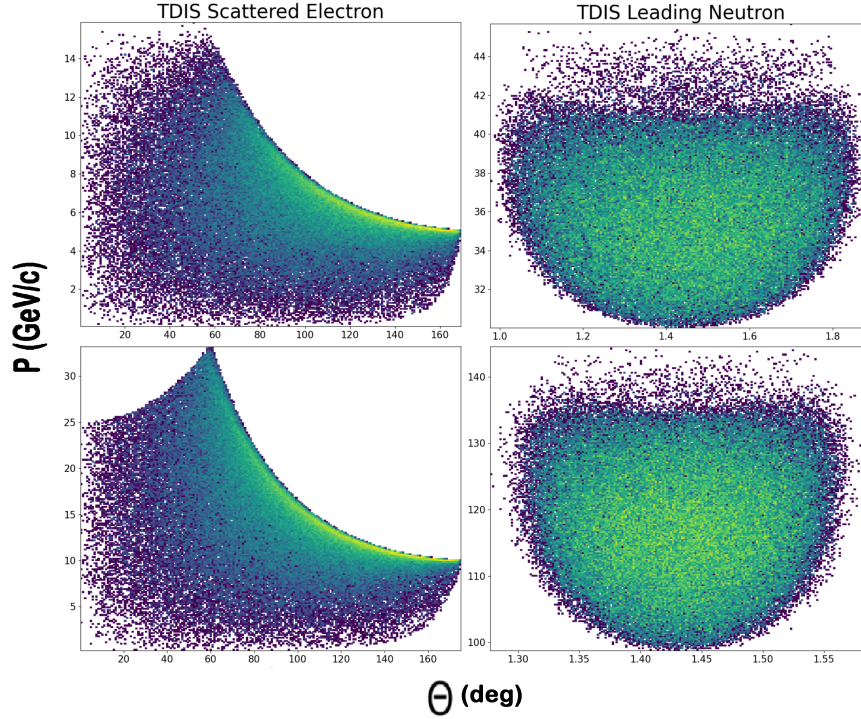
4.2.  $e p \rightarrow e' + X + n$ .

Figure 11: A comparison of the scattered electron (left) and leading neutron (right) kinematics for two energy settings -  $10 \times 135$  (bottom) and  $5 \times 41$  (top). The momentum,  $P$ , and angle,  $\theta$ , are defined in the lab frame. In both cases, the scattered electrons are within the acceptance of the central detector and the leading neutrons are at small forward angles and carry most of the proton beam energy after the scattering process.

The initial pion structure studies were conducted at the highest energy of  $18 \times 275$  (corresponding to the electron and proton beam energy, respectively, both in GeV) to maximise the kinematics coverage. However, to improve access to the high  $x_\pi$  region, alternate lower beam energies  $10 \times 135$  and  $5 \times 41$  were also selected. These lower beam energies allow access to this high  $x_\pi$  regime over a wider range of  $Q^2$ . For a comparison, the  $18 \times 275$  energies allow access to high  $x_\pi$  data over a  $Q^2$  range of  $\sim 200 - 1000 \text{ GeV}^2$ , while with the  $10 \times 135$  energies that range was increased to  $\sim 30 - 1000 \text{ GeV}^2$ , and with the  $5 \times 41$  energies to  $\sim 5 - 1000 \text{ GeV}^2$ . The lower-energy combination of  $5 \times 41$  is

even more beneficial for tagging kaon structure by allowing detection of the leading  $\Lambda$  events.

The kinematics for the more advantageous lower energy settings,  $10 \times 135$  and  $5 \times 41$ , are shown in figure 11. While the scattered electrons are within the acceptance of the central detector, the leading neutrons for these two energy settings are at a very small forward angle while carrying nearly all of the proton beam momentum. These leading neutrons will be detected by the ZDC.

Figure 12 shows the acceptance plots for neutrons in the ZDC for all three energy settings. As one can see, the spatial resolution of the ZDC plays an important role for the highest energy setting, since it is directly related to the measurements of  $p_T$  or  $t$ . For the lowest energy setting, the total acceptance coverage of the ZDC is important. This sets a requirement for the total size of ZDC to be a minimum of  $60 \times 60 \text{ cm}^2$ . Such a configuration of the ZDC provides nearly 100% neutron detection efficiency for this channel.

### 4.3. $\Lambda$ tagging

For the case of a leading  $\Lambda$  event, to elastic or DIS scattering from a kaon, both  $\Lambda$  decay products must be detected at small forward angles owing to the nature of two-body decay kinematics. The detection of these decay products requires high-resolution and granularity because of the small angle of separation of decay products.

Detection of the decay channel  $\Lambda \rightarrow n + \pi^0$  is feasible, but will require electromagnetic calorimetry before the ZDC to distinguish the neutron and the two photons coming from  $\pi^0$  decay. Detection of the other decay channel,  $\Lambda \rightarrow p + \pi^-$ , poses a more challenging measurement owing to its requirement of additional charged-particle trackers or a veto trigger on the path to ZDC.

The reconstruction of the  $\Lambda$  event in the far-forward detection area is one of the most challenging tasks. This comes mainly from the fact that these leading  $\Lambda$ s have energy close to the initial beam energy, and thus their decay lengths can be tens-of-metres along the Z-axis (or beam line). This complicates detection of the decay products; hence, the final  $\Lambda$  mass reconstruction.

Figure 13 illustrates this further, showing the Z-coordinate of where the  $\Lambda$ -decay occurs for different beam energies. For the lower beam energy settings ( $5 \times 41$ ) most  $\Lambda$  decays are within the central detector region, but at the higher proton (ion) beam energies the  $\Lambda$  decays happen more in the forward-detection area, with tails of the

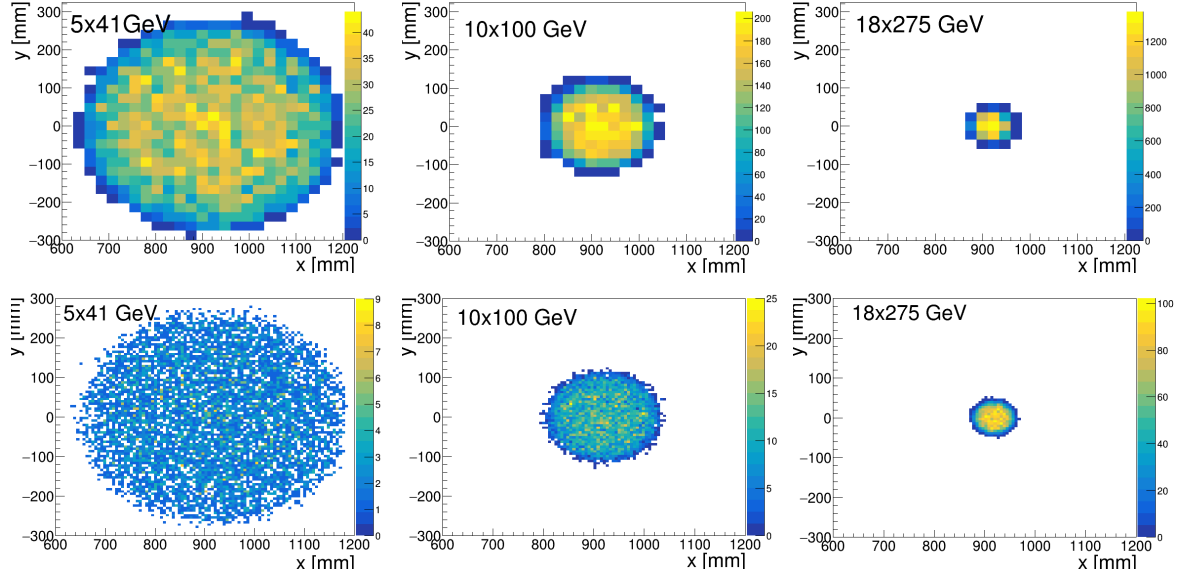


Figure 12: Acceptance plot for neutrons in the  $60 \times 60$  cm<sup>2</sup> ZDC, with a low spatial resolution of 3 cm (upper panels) and with a high spatial resolution of 0.6 cm (lower panels), for different energy settings, from left to right, of  $5 \times 41$ ,  $10 \times 100$ , and  $18 \times 275$ . The acceptance plot for  $5 \times 100$  would be similar as shown for  $10 \times 100$ . The lower proton (ion) energies set the requirement for the size of the ZDC, whereas the higher proton (ion) energies drive the spatial resolution requirement.

decay process reaching to near the ZDC location. Table 2 shows the percentage of decayed  $\Lambda$  for different energies and different Z ranges:  $Z_{vtx} < 5$  m,  $5 \text{ m} < Z_{vtx} < 30$  m and  $Z_{vtx} > 30$  m.

$E_{\text{beams}}$	$Z_{vtx} < 5$ m	$5 \text{ m} < Z_{vtx} < 30$ m	$Z_{vtx} > 30$ m
$5 \times 41$	83.0%	16.6%	0.4%
$10 \times 100$	52.1%	46.7%	1.2%
$18 \times 275$	23.3%	56.2%	20.5%

Table 2: Percentage of decayed  $\Lambda$ 's in different detection ranges.

To study the possibility of  $\Lambda$  mass reconstruction further, both main decay modes

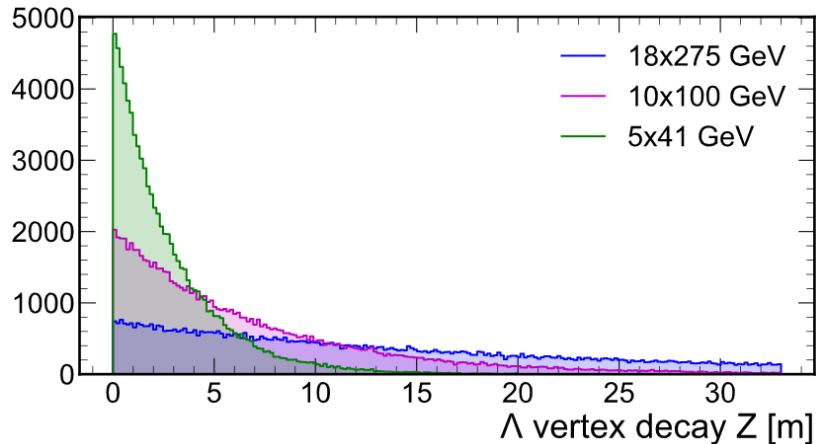


Figure 13: The  $\Lambda$ -decay spectrum along the beam line for different beam energies.

have been examined:  $\Lambda \rightarrow p+\pi^-$ , with a branching ratio of 63.9%, and  $\Lambda \rightarrow n+\pi^0$ , with a branching ratio of 35.8%. Both channels can be cleanly separated by the different charge of the final-state particles, and thus by the different detector components that will play a role in their detection.

*4.3.1.  $\Lambda \rightarrow p+\pi^-$ .* For this process, there are only charged particles in the final state. Therefore, one must rely on sub-components along the far-forward area, such as the B0 tracker, the Off-Momentum trackers, and Roman Pots for detection and reconstruction of the decay products.

As an example, occupancy plots for the beam-energy setting of  $5\times 41$  are shown in figure 14. Since this is the lowest beam-energy setting, most of the  $\Lambda$ s would decay in the first metre (before the B0 magnet), and the  $\Lambda$  decay products are expected to have low momenta. Therefore, as expected, protons coming from the  $\Lambda$  decays will mostly be detected, owing to their lower rigidity, in the off-momentum detectors (c) and partially in a B0 tracker (b). While for pions, the tracker inside the B0 dipole will be the only detecting element (a). As one can also see from this figure, the proton-beam-pipe aperture inside the B0-dipole plays an important role and sets the detection efficiency for pions, as well as the azimuthal angle  $\phi$ -coverage of the detecting elements around the proton beam-pipe. Further information on the distributions for detected decay products at these lower beam energies of  $5\times 41$  are given in figure 15.

For the higher beam-energy settings, e.g.  $10\times 100$ , the protons are to be detected

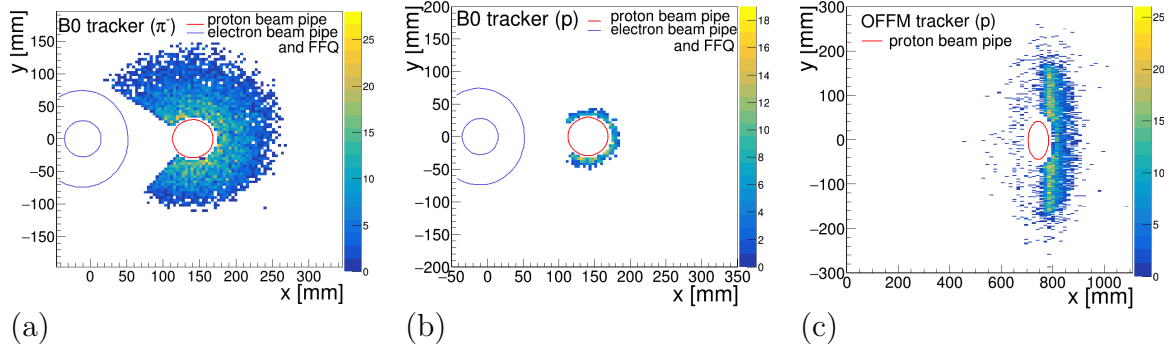


Figure 14: Occupancy plots for energy setting  $5 \times 41$  (a) for  $\pi^-$  in the B0 tracker, (b) for protons in the B0 tracker and (c) for protons in the Off-Momentum detectors. The red circle shows the beam pipe position and the blue circle shows the electron final-focus quadrupole (FFQ) aperture inside the B0 dipole.

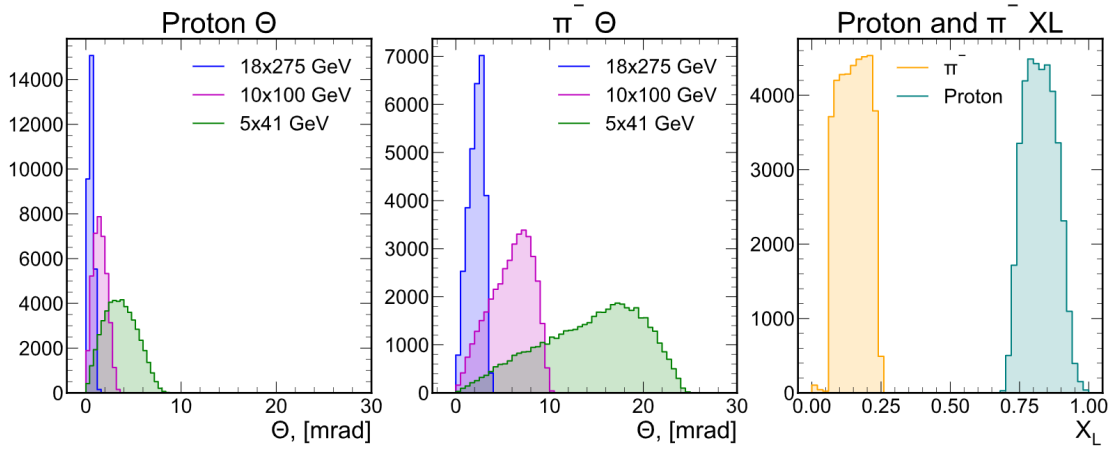


Figure 15: Theta and  $x_L$  distributions for detected decay products of  $\Lambda$  particles for different beam energy combinations. Proton theta (left),  $\pi^-$  theta (center), proton and  $\pi^-$   $x_L$  (right).

in the roman-pots (and partially in Off-Momentum detectors), see figure 16. Pions originating from a  $\Lambda$ -decay with  $Z_{vxt} < 4$  m will only partially be detected in the B0-area, while most of them will go undetected through the proton beam pipe. Pions with higher momentum and lower angles ( $p_t$  or theta) can pass through the bores of the FFQs and be detected in the Off-Momentum detectors. Their detection represents the

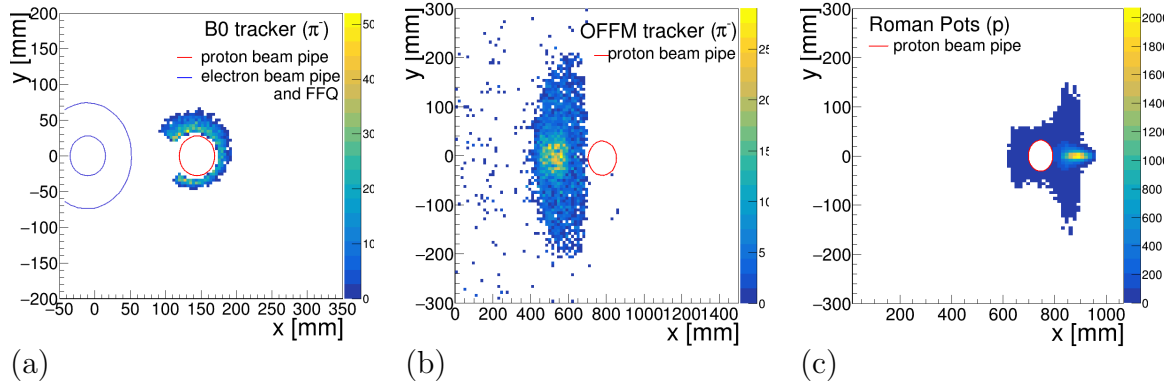


Figure 16: Occupancy plots for energy setting  $10 \times 100$  (a) for  $\pi^-$  in the B0 tracker, (b) for  $\pi^-$  in the Off-Momentum tracker, and (c) for protons in the Roman Pots detectors. The red circle shows the beam pipe position and the blue circle shows the electron beam FFQ aperture inside the B0 dipole.

denser (light) area of detection in the Off-Momentum detectors (figure 16(b)). Note that owing to the negative charge of the pions, they will experience an opposite bending in dipoles, as compared to protons (compare with the protons in the Off-Momentum detectors on figure 14(b)). Therefore, in order to detect the  $\Lambda$ -decays in this channel, the Off-Momentum detectors need to provide a full azimuthal coverage, to establish a proper detection for the negatively-charged particles.

For the  $5 \times 41$  beam-energy combination, figure 17 shows the momentum (top panels) and angular (bottom panels) distributions of protons (left panels) and pions (right panels) from  $\Lambda$ -decay as a function of distance from the  $\Lambda$ -decay point, as detected in one of the beam line sub-detectors. This in turn illustrates which of the sub-detectors along the beam line detects the decay products. The protons carry most of the initial proton beam momentum and extend over the far-forward direction, with angles less than 8 mr. On the other hand, as one can clearly see from the high density of hits, the  $\Lambda$ -reconstruction efficiency will mainly depend on the efficiency for the detection of pions in the B0 area, with angles in the 5-25 mr range.

For the higher beam energy combination, for example  $10 \times 100$ , the situation will be much different. Figure 18) shows the momentum and angular distributions for protons and  $\pi^-$ . For the latter, one can clearly see a “dead” area appear along the beam line, where the FFQ beam elements are located, prohibiting placement of detectors and

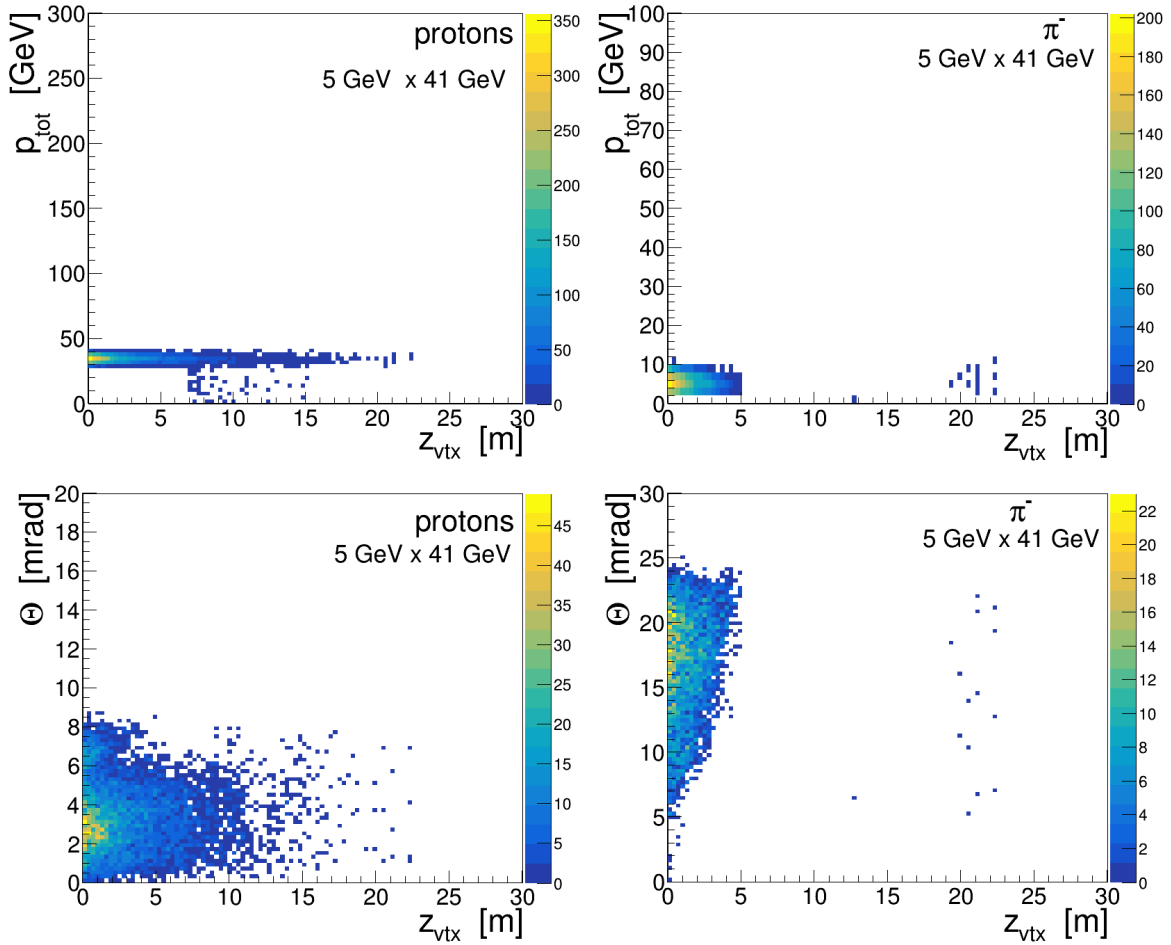


Figure 17: Momentum (top) and angular (bottom) distributions of protons (left) and  $\pi^-$  (right) from the  $\Lambda \rightarrow p + \pi^-$  decay at beam-energy setting  $5 \times 41$ , as registered in the far-forward detectors as a function of their origination (the decay vertex).

thus  $\pi^-$  detection. This comes from the fact that these pions have significantly lower momentum and so are swept into the magnets and beam line. Those  $\Lambda$ s which decay after the set of FFQs will be tagged by the off-momentum detector, but since the  $Z_{vtx}$  is unknown, it will be difficult to make a one-to-one correlation between the tagged position and the particle's momentum or angle. Therefore, for the final reconstruction of the  $\Lambda$  invariant mass, one has to use only events with  $Z_{vtx} < 3$ -5 metres, to make this correlation possible. That this remains possible is revealed in figure 19–right, which

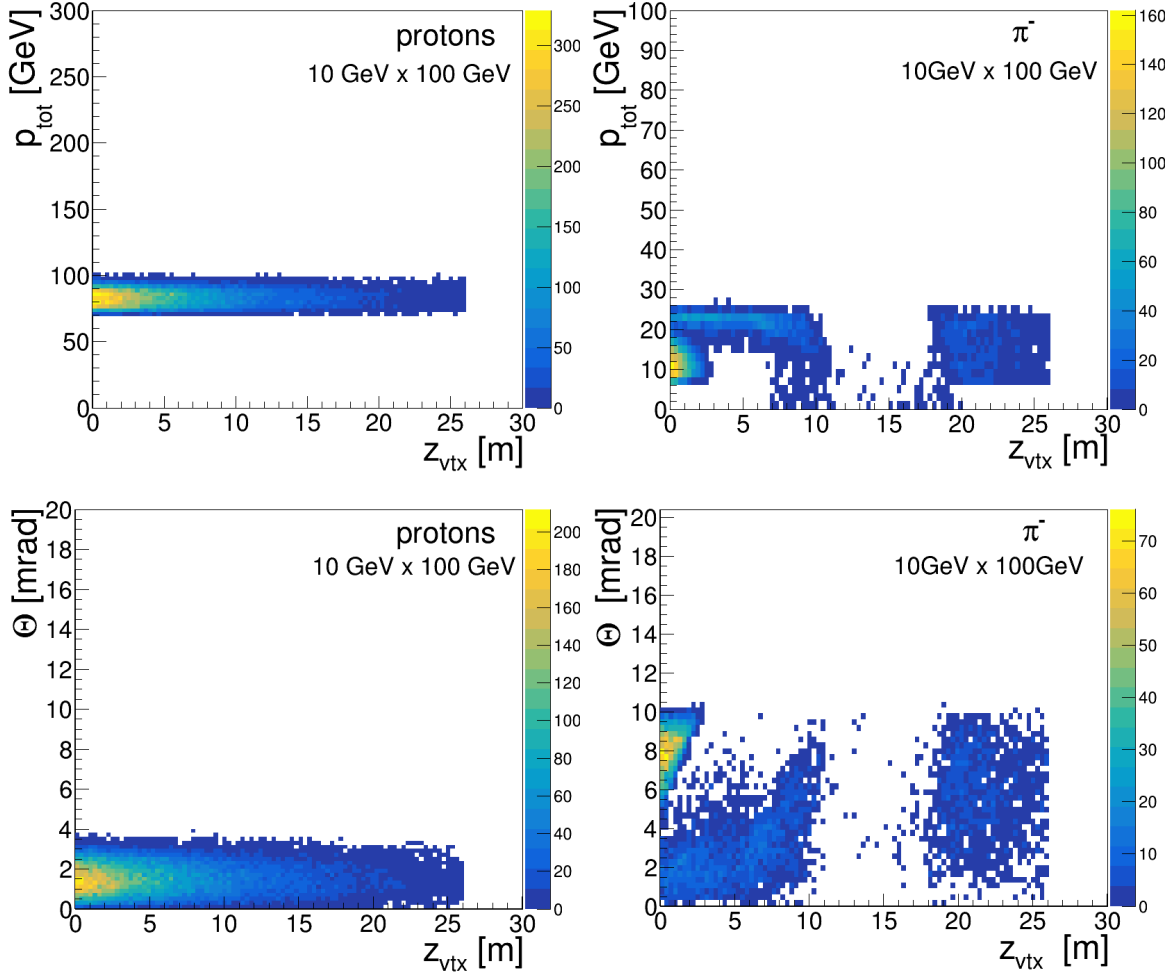


Figure 18: Momentum (top) and angular (bottom) distributions of protons (left) and  $\pi^-$  (right) from the  $\Lambda \rightarrow p + \pi^-$  decay at beam-energy setting  $10 \times 100$ , as registered in the far-forward detectors as a function of their origination (the decay vertex). For the  $\pi^-$ , one clearly sees the “dead” area in the FFQ magnet region, where placement of detectors is impossible.

shows the invariant mass spectra of the  $\Lambda(p, \pi^-)$  channel for this  $10 \times 100$  beam energy setting. The corresponding  $p_T$  spectrum of the  $\Lambda$  particles is shown on the left panel of figure 19.

We summarise this result in table 3, which shows the expected  $\Lambda$  detection



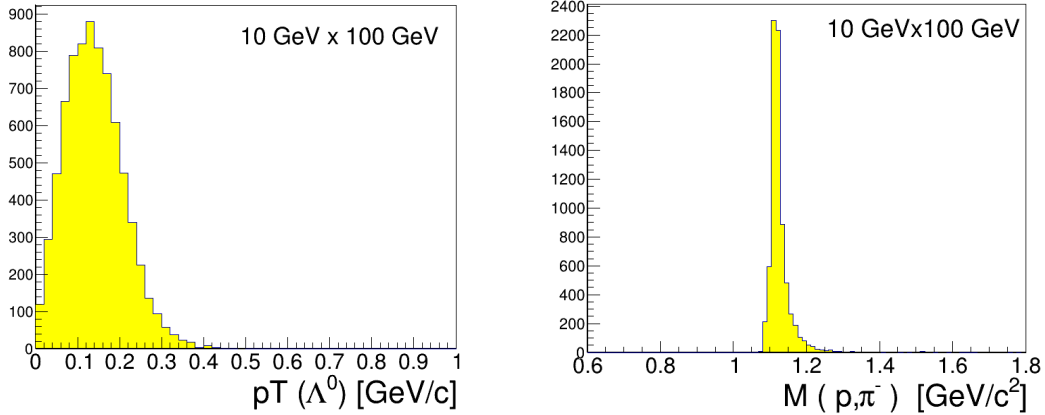


Figure 19:  $p_T$  (left) and invariant mass (right) of reconstructed  $\Lambda$  particles for the  $10 \times 100$  beam energy setting.

efficiency for the decay  $\Lambda \rightarrow p + \pi^-$ . A cut on decay within 4 meters,  $Z_{vtx} < 4$  m has been applied for this selection. The decrease in detection efficiency for the higher-energy settings comes mainly from this  $Z_{vtx}$  cut, but is necessary to ensure  $\Lambda$  mass reconstruction.

Beam energies	$5 \times 41$	$10 \times 100$	$18 \times 275$
Lambda Efficiency	20%	15%	1%

Table 3:  $\Lambda$  detection efficiency as a function of energy setting, for  $\Lambda$  detection with a cut on decay applied of  $Z_{vtx}$  cut  $< 4$  m to ensure  $\Lambda$ -mass reconstruction.

4.3.2.  $\Lambda \rightarrow n + \pi^0$ . For this process, there are only neutral particles in the final state. The main scheme of detection for these particles will be the ZDC and/or some kind of electromagnetic calorimeter/photon detector in the B0 area. As with the  $p + \pi^-$  decay mode, with lower beam energies, more particles can be detected in the central detector region. Figure 20 shows the angular ( $\Theta$ ) distributions for  $n$  and  $\pi^0$  for different beam energies. It is furthermore assumed that the  $\pi^0$  is reconstructed from  $\pi^0 \rightarrow \gamma\gamma$ , where the photons are deposited in one of the corresponding detectors.

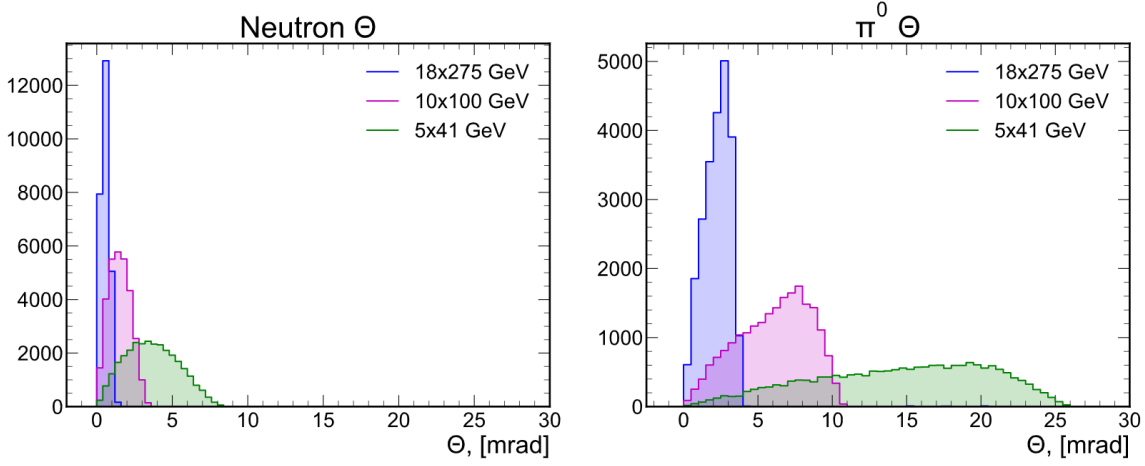


Figure 20: Angular distributions for detected decay products of  $\Lambda \rightarrow n + \pi^0$ : (a) neutrons; and (b)  $\pi^0$ . Beam energy settings:  $18 \times 275$ ,  $10 \times 100$ , and  $5 \times 41$ .

The energy and angular distributions of the two photons from the  $\pi^0$  decay are shown in figure 21, for various beam energy settings. At lower beam energy settings, some measurement to detect the larger-angle photons in the B0 area is required to recapture efficiency. As the beam energy increases, the ZDC starts playing the main role for detection of both neutrons and neutral-pions. This is illustrated further in figure 22, which shows the occupancy plots of the ZDC for both neutrons and the  $\gamma\gamma$  from  $\pi^0$  decay for different energy settings. At the higher  $10 \times 135$  energies, the ZDC captures all photons from neutral-pion decay, while at the lower  $5 \times 41$  energies many photons are at larger angles reducing the detection fraction in the ZDC.

#### 4.4. Exclusive $p(e, e'\pi^+n)$ events

The kinematic distributions for exclusive  $p(e, e'\pi^+n)$  events are shown in figure 23. As for tagged DIS events, the neutrons assume nearly all of the proton beam momentum, and need to be detected at very forward angles in the ZDC. The scattered electrons and pions also have similar momenta as in the tagged DIS case, except that here the electrons are distributed over a wider range of angles. For instance, at the  $5 \times 100$  beam-energy setting, the 5 – 6 GeV electrons are primarily scattered  $25^\circ - 45^\circ$  from the electron beam, while the 5 – 12 GeV  $\pi^+$  are at  $7^\circ - 30^\circ$  from the proton beam. Further details of the exclusive events study, including the assumed requirements to separate

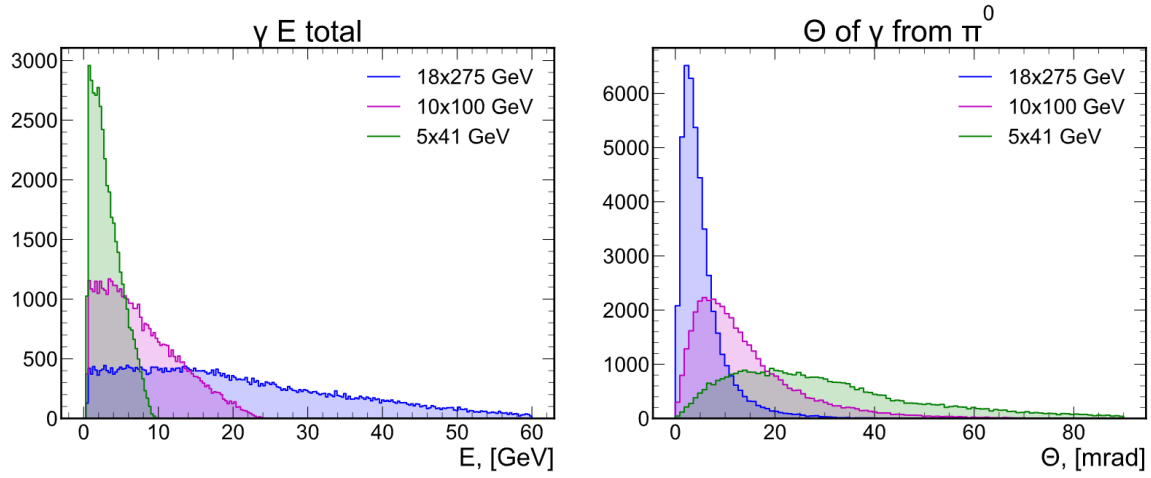


Figure 21: Energy and angular  $\Theta$  distributions for the detected  $\gamma\gamma$  to reconstruct the  $\pi^0$  from a  $\Lambda$  decay channel

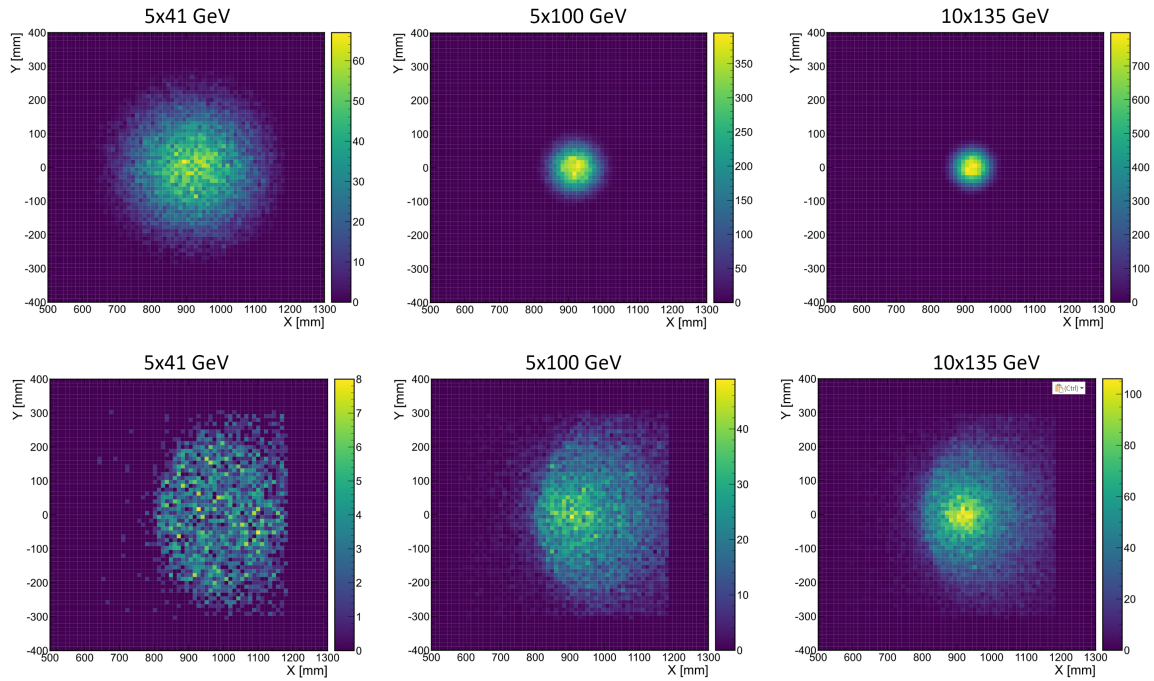


Figure 22: Occupancy distribution for neutrons (top panels) and  $\gamma\gamma$  from  $\pi^0$  decay (bottom panels) as detected in the ZDC for different beam energy settings.

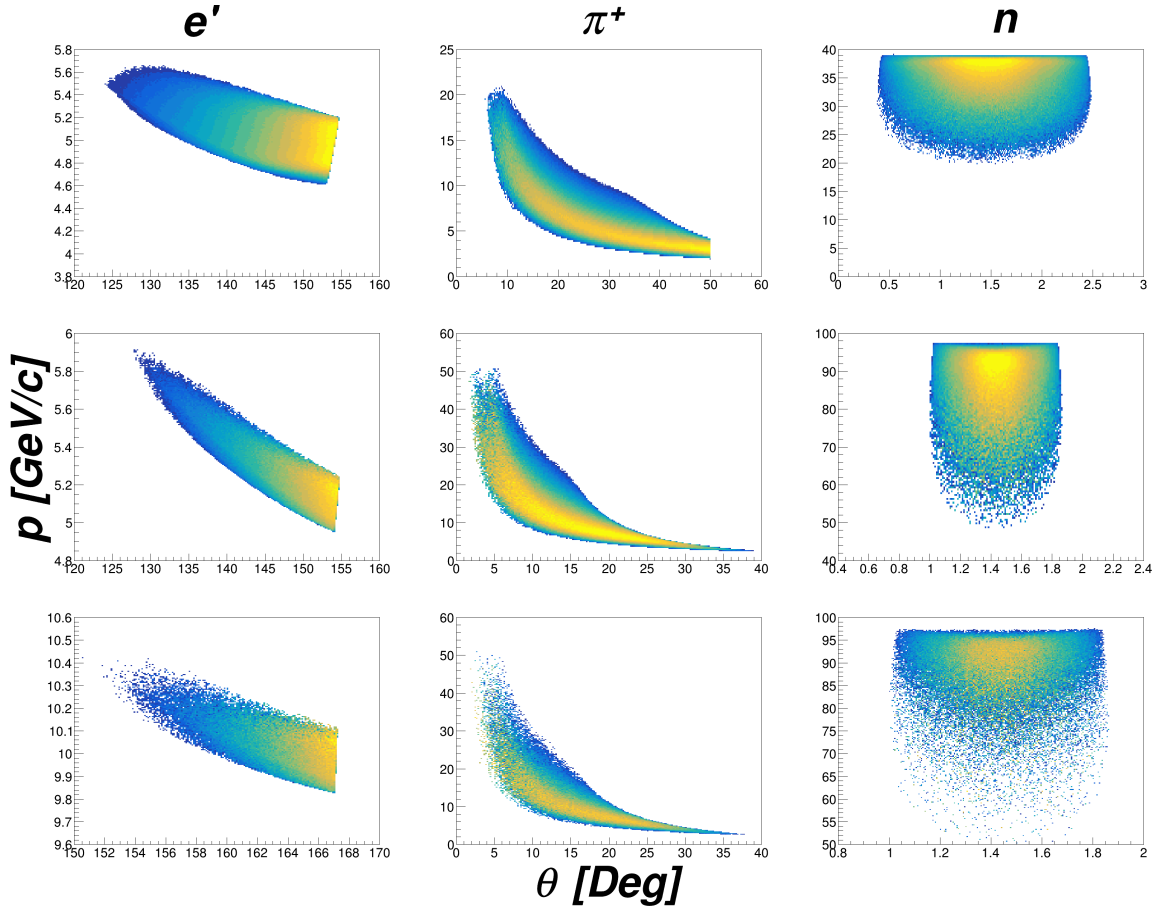


Figure 23: Kinematic distributions for exclusive  $p(e, e'\pi^+n)$  events for  $e'$  (left),  $\pi^+$  (center), and  $n$  (right), at  $5 \times 41$  (top),  $5 \times 100$  (middle), and  $10 \times 100$  (bottom) beam energies. The neutron distribution is offset by 25 mr owing to the beam crossing angle.

exclusive events from non-exclusive background, and the pion form factor projections, are given in section 5.2.

#### 4.5. Accelerator and instrumentation requirements

The physics simulation examples show that access to meson structure benefits greatly from EIC operations at the lower center-of-mass energies, with both  $ep$  and  $ed$  measurements at similar cm energies. Lower energies enhance the range of  $Q^2$  at large  $x_\pi$ . Lower energies allow detection to uniquely tag kaon structure: this enhances

$\Lambda$  decay probability at short distances and permits  $\Lambda$ -mass reconstruction to work from the detected decay products. To tag meson structure, proper instrumentation of B0 tracking detectors is needed, with full azimuthal coverage and perhaps a smaller proton-beam pipe diameter. Off-momentum detectors also have to provide full azimuthal coverage for detection of negatively-charged decay particles.

In terms of complimentary, an improved spectrometer along the beam line to enhance efficiency for detection of the low-momenta decay particles would be beneficial. The present beam line design leaves a large area with no possible detection, making  $\Lambda$  tagging difficult for particles originating from larger  $Z_{\text{vtx}}$ . This complicates access to meson structure at larger proton (ion) beam energies. Alternatively, a beam line design with an improved secondary focus could be beneficial for  $\Lambda$  tagging.

## 5. Physics projections

### 5.1. Meson structure functions

*5.1.1. Pion structure function projections* A fast Monte Carlo was used for feasibility studies of  $\pi$  and  $K$  structure function measurements. The Monte Carlo is a C++ and ROOT based custom event generator [178] that uses the random number generator TRandom3 in ROOT. The inputs of the generator are minimum and maximum  $Q^2$  and  $x$  values, initial ion and electron beam energies, flags for initial beam smearing, and the number of events to simulate. The generator calls various quantities such as CTEQ6 PDF tables, nucleon structure functions, and the tagged  $\pi$  and  $K$  structure functions and splitting functions. The  $\pi$  structure function, in particular, can be parametrised in many ways. Here, the  $F_2^\pi$  structure function is calculated at NLO through the use of pion PDFs, which were determined in [144].

The hadronic splitting function,  $f_i$ , appearing in Eq. (10) determines the meson flux essential to computing the leading-baryon production cross section of equation (9). For the sake of the simulations presented in this analysis, this flux was computed in the context of the single-meson exchange framework, which is valid for soft exchange momenta. The details of the hadronic splitting function were fixed to the relativistic vertex factor approach used in [142], including a  $s_{\pi N}$ -dependent Gaussian interaction with ultraviolet regulator  $\Lambda \sim 1 \text{ GeV}$ . Although the details of the hadronic splitting were not varied in simulating EIC tagging measurements, it should be stressed that the EIC can be expected to be sensitive to the meson flux as well as the meson structure

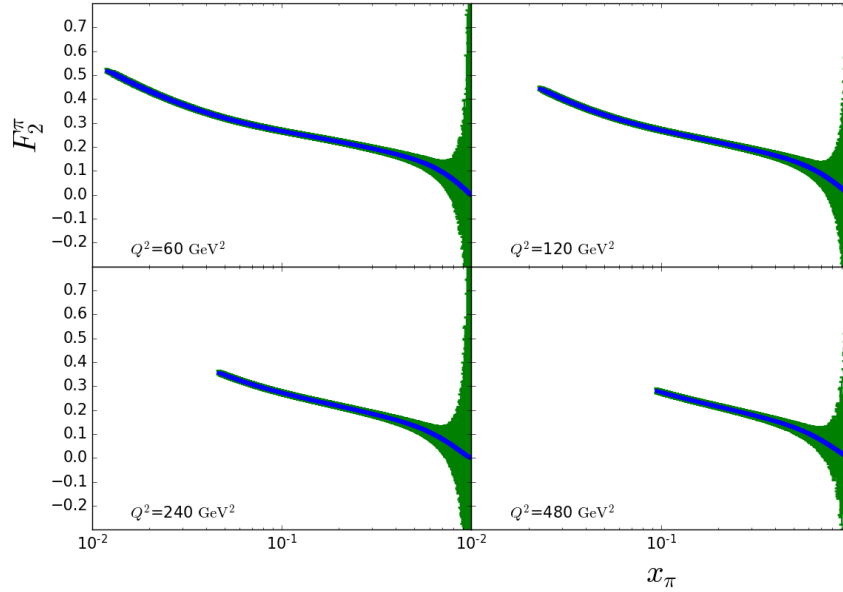


Figure 24: Monte Carlo projections of the pion structure function vs  $x$  for a beam energy of  $10 \times 135$ . The projected data is binned in  $x$  and  $Q^2$ , with bin sizes of 0.001 and  $10 \text{ GeV}^2$ , respectively. The blue points are the Monte Carlo projections for  $Q^2$  values of 60, 120, 240,  $480 \text{ GeV}^2/c$ . The green bands are the statistical uncertainties for a luminosity of  $100 \text{ fb}^{-1}$ .

function. A detailed examination of the sensitivity to the meson flux will be undertaken in the future.

The plot in figure 24 shows the reach in  $x$  for four  $Q^2$  bins at the  $10 \times 135$  energy setting. The pion structure function simulations were validated by their agreement with the experimental HERA data [126] in that regime, and with the GRV fit [121] at higher  $x$ . Statistical uncertainties with the addition of the leading neutron detection fraction (discussed in the previous section) were incorporated to the overall uncertainty for a luminosity of  $\mathcal{L} = 100 \text{ fb}^{-1}$ . For this energy, the coverage in  $x$  extends down to  $10^{-2}$ , with reasonable uncertainties in the mid-to-large  $x$  region, increasing rapidly as  $x \rightarrow 1$ . Even with these restrictions, the coverage in mid to high  $x$  is unprecedented and should allow for detailed comparisons between pion and kaon structure.

In Figure 7 we showed the impact of EIC data on the pion PDFs themselves and

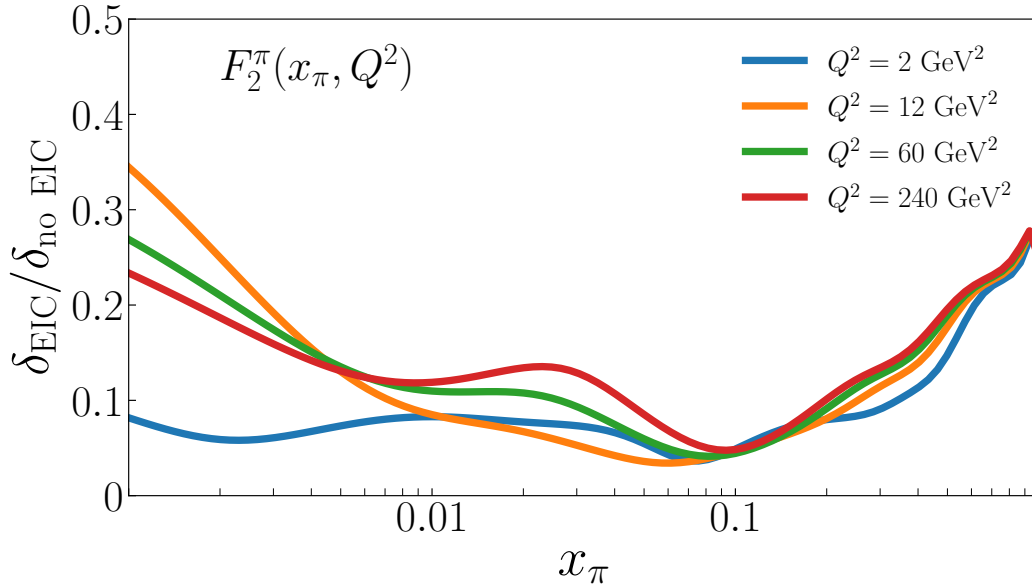


Figure 25: Ratio of the uncertainty of the  $F_2^\pi$  structure function from the global fit with and without including EIC projected data to the uncertainty of the  $F_2^\pi$  as a function of  $x_\pi$  for various  $Q^2$  values.

their uncertainties, folding in the estimated systematic uncertainty and the projected statistical uncertainties from the simulations (see Figure 8). The resulting access to a significant range of  $Q^2$  and  $x$ , for appropriately small  $-t$ , will allow for much-improved insights in the gluonic content of the pion.

Figure 25 displays the ratio of the uncertainty of the  $F_2^\pi(x_\pi, Q^2)$  structure function resulting from a global fit with EIC projected data to that without it. We show various  $Q^2$  values of a wide range between a few  $\text{GeV}^2$  and a few hundred  $\text{GeV}^2$  over the range  $10^{-3} < x_\pi < 1$  to investigate the  $Q^2$  dependence of the impact. Strikingly, the  $F_2^\pi$  structure function's uncertainties reduce by 80-90% in the range of  $x_\pi$  between  $3 \times 10^{-3}$  and 0.4 in the presence of EIC data, no matter the values of  $Q^2$ . Within the whole range, the uncertainties reduce by 65% or more. Below  $x_\pi$  of 0.1, the  $F_2^\pi$  structure function reduces by a factor of 10 for the case when  $Q^2 = 2 \text{ GeV}^2$ . The constraining power at such low values of  $Q^2$  is illustrated in figure 8, where all data points shown are in the range  $Q^2 < 10 \text{ GeV}^2$ . The EIC provides a unique opportunity to improve

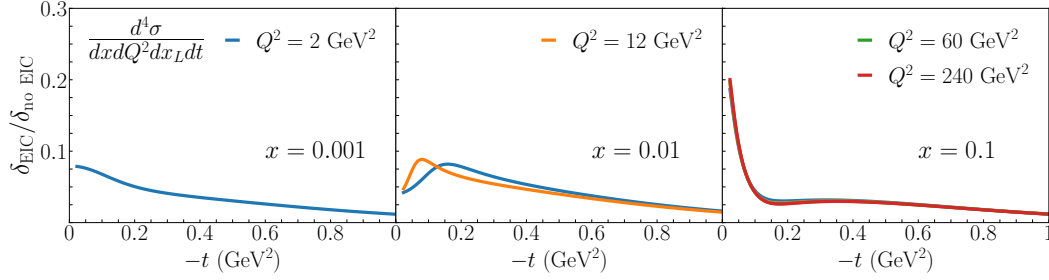


Figure 26: Ratios of the uncertainty of the differential cross section  $\frac{d^4\sigma}{dx dQ^2 dx_L dt}$  from the global fit including EIC projected data to the uncertainty of that without the EIC as a function of  $-t \in [-t_{\min}, 1]$  for various  $Q^2$  and for (*left panel*)  $x = 0.001$ , (*middle panel*)  $x = 0.01$ , and (*right panel*)  $x = 0.1$ . For all calculations, the value  $x_L = 0.85$  was used.

our knowledge of the  $F_2^\pi$  over a large range in  $Q^2$  and  $x$ .

As discussed in section 3.1, theoretical calculations [43] predict that the Sullivan process should provide clean access to meson structure below a minimum value of  $-t$ . For the pion, this is  $-t \leq 0.6$  GeV<sup>2</sup>. Similar, corrections for extracting the pion structure information from the theoretical backgrounds (absorptive corrections, higher meson-mass exchanges, etc., see section 3.2) are minimized by measuring at the lowest  $-t$  possible. Experimentally, this can be addressed by various tagged pion structure measurements as function of  $-t$ , for low  $-t < \sim 0.6$  GeV<sup>2</sup>, and verifying pion structure extraction.

Figure 26, shows the reduction of the uncertainties of the four-fold differential cross section,  $\frac{d^4\sigma}{dx dQ^2 dx_L dt}$ . The impact is illustrated by means of the ratio of cross sections, including EIC projected data to the uncertainty of that without the EIC, as a function of  $-t$  and up to  $-t = 1$ . The left and middle panels of figure 26, show that as a function of  $-t$ , the uncertainties on the differential cross section reduce by 90% at  $x = 0.001$  and  $x = 0.01$ . For the case when  $x = 0.1$  in the right panel the values of  $Q^2$  are insignificant in the ratio of uncertainties. At large  $Q^2$ , at  $x \sim 0.1$ , the ratio of uncertainties rises when  $-t$  is closer to 0 which is due to a reduced experimental phase space to the low  $-t$  region for those kinematics. The overall impact of >75% improvement on the uncertainties indicates both that our knowledge currently is poor and that the EIC will provide good constraints for cross sections. Furthermore, this



underlines that the measured tagged cross sections as function of  $-t$  can be used to confirm robustness of pion structure extraction.

*5.1.2. Kaon structure function and splitting function projections* The pion structure function analysis presented here can be extended to the kaon, as the single-meson exchange framework can be generalised to the flavour SU(3) sector with expected validity for soft exchange kaons. Empirical knowledge of the kaon sector is even more sparse than the analogous information on the pion. As such, comprehensive data would be of great utility for unravelling the splitting function ratio,  $f_K/f_\pi$  as well as the structure function of the kaon,  $F_2^K$ . For initial simulations, the splitting function  $f_K$  might be fixed at first-order to inclusive hadroproduction data, and  $\Lambda(\text{uds})$  baryon production according to equation (9). Ultimately, precise EIC data over a range of  $x$ ,  $Q^2$ ,  $y$ , and  $t$  would be instrumental for the sake of unraveling and constraining the meson flux model from the structure function  $F_2^K$ .

## 5.2. Meson form factors

The experimental determination of the  $\pi^+$  electric form factor ( $F_\pi$ ) is challenging. The best way to determine  $F_\pi$  would be electron-pion elastic scattering. However, the lifetime of the  $\pi^+$  is only 26.0 ns. Since  $\pi^+$  targets are impossible and  $\pi^+$  beams with the required properties are not yet available for measurements at modest-to-large  $Q^2$  values, one must employ exclusive electroproduction,  $p(e, e'\pi^+)n$ . This is best described as quasi-elastic ( $t$ -channel) scattering of the electron from the virtual  $\pi^+$  cloud of the proton, where  $t$  is the Mandelstam momentum transfer  $t = (p_p - p_n)^2$  to the target nucleon. As discussed in section 3.1, scattering from the  $\pi^+$  cloud dominates the longitudinal photon cross section ( $d\sigma_L/dt$ ) at sufficiently small  $-t$ .

To reduce background contributions, one normally separates the components of the cross section owing to longitudinal (L) and transverse (T) virtual photons (and the LT, TT interference contributions) via a Rosenbluth separation. However, L/T separations are impractical at the EIC, as one cannot reach sufficiently low  $\epsilon$  data to provide a good lever arm. Below, we propose an alternate technique to access  $\sigma_L$  via a model, validated with exclusive  $\pi^-/\pi^+$  ratios from deuterium. Once  $d\sigma_L/dt$  has been determined over a range of  $-t$ , from  $-t_{\min}$  to  $-t \approx 0.6 \text{ GeV}^2$ , the value of  $F_\pi(Q^2)$  is determined by comparing the observed  $d\sigma_L/dt$  values with the best available electroproduction model, incorporating off-shell pion and recoil nucleon effects. In principle, the obtained

$F_\pi$  values depend upon the model used, but one anticipates this dependence to be reduced at sufficiently small  $-t$ . Measurements over a range of  $-t$  are essential as part of the model validation process. The JLab 6 GeV experiments were instrumental in establishing the reliability of this technique up to  $Q^2 = 2.45 \text{ GeV}^2$  [23, 38, 39, 179–184], and extensive further tests are planned as part of JLab experiment E12-19-006.

*5.2.1. Requirements for separating exclusive and SIDIS events.* The exclusive  $\pi^+$ -channel cross section is several orders of magnitude smaller than the neighbouring SIDIS background; but it is distributed over a much narrower range of kinematics, and this is essential for the separation of the exclusive events from the background. The exclusive  $p(e, e'\pi^+n)$  reaction is isolated by detecting the forward-going high-momentum neutron, i.e.  $e - \pi^+ - n$  triple coincidences. Since the neutron energy resolution is not very good, the neutron hit is used as a tag for exclusive events. The neutron momentum is otherwise not used in the event reconstruction.

Detector effects have been simulated via the following ad-hoc smearing functions. The pion and electron angular resolutions were estimated by assuming a  $10 \mu\text{m}$  position resolution in a cylindrical silicon vertex tracker (comparable with ZEUS), and this Cartesian position uncertainty was propagated to polar coordinates  $(\theta, \phi)$ . From this,  $\delta p = 250 \mu\text{rad}$  was conservatively assumed for all angles, for both the electron and the pion. The pion and electron momentum resolution was estimated from track reconstruction in the magnetic field via the resolution in [185], assuming 5 position measurements in a 3T solenoidal field. To simplify the MC study,  $\delta p/p = 2\%$  was conservatively assumed for all angles, for both the electron and the pion. Since the neutron energy resolution in the ZDC is not very good, the neutron hit was used as a tag for deep exclusive meson production (DEMP) events. The neutron momentum was not otherwise used in the event reconstruction. Thus, the missing momentum is calculated as  $p_{miss} = |\vec{p}_e + \vec{p}_p - \vec{p}_{e'} - \vec{p}_\pi|$ .

The effectiveness of kinematic cuts to isolate the exclusive  $\pi^+$  channel was evaluated by comparison with a simulation of  $p(e, e'\pi^+)X$  SIDIS events, including both detector acceptance and resolution smearing effects. The most effective cuts are on the detected neutron angle ( $\pm 0.7^\circ$  from the outgoing proton beam), the reconstructed  $-t < 0.5 \text{ GeV}^2$ , and the missing momentum defined above. The  $p_{miss}$  cut is  $Q^2$ -bin dependent, where the value is chosen to optimize the signal/background ratio for each bin. It ranges from  $p_{miss} > 95 \text{ GeV}/c$  at  $Q^2 = 6 \text{ GeV}^2$ , to  $77 \text{ GeV}/c$  at  $Q^2 = 35 \text{ GeV}^2$ , where all events are removed above the cut value. After application of these cuts, the

exclusive  $p(e, e'\pi^+n)$  events are cleanly separated from the simulated SIDIS events.

*Determining the longitudinal cross section  $d\sigma_L/dt$ .* After the exclusive  $\pi^+n$  event sample is identified, the next step is to separate the longitudinal cross section  $d\sigma_L/dt$  from  $d\sigma_T/dt$ , needed for the extraction of the pion form factor. However, a conventional Rosenbluth separation is impractical at the EIC owing to the very low proton beam energy required to access  $\epsilon < 0.8$ . Fortunately, at the high  $Q^2$  and  $W$  values accessible at the EIC, phenomenological models predict  $\sigma_L \gg \sigma_T$  at small  $-t$ . For example, the Regge-based model in [186] predicts  $R = \sigma_L/\sigma_T > 10$  for  $Q^2 > 10 \text{ GeV}^2$  and  $-t < 0.06 \text{ GeV}^2$ , and  $R > 25$  for  $Q^2 > 25 \text{ GeV}^2$  and  $-t < 0.10 \text{ GeV}^2$ . Thus, transverse cross section contributions are expected to be 1.3–14%, with the ratios becoming more favourable with increasing  $Q^2$  and decreasing  $-t$ . The most practical choice appears to be to use a model to isolate the dominant  $d\sigma_L/dt$  from the unseparated cross section  $d\sigma_{\text{uns}}/dt$ .

To control the systematic uncertainty associated with the theoretical correction to estimate  $\sigma_L$  from  $\sigma_{\text{uns}}$ , it is very important to confirm the validity of the model used. This can also be done with EIC data, using exclusive  ${}^2H(e, e'\pi^+n)n$  and  ${}^2H(e, e'\pi^-p)p$  data in similar kinematics to the primary  $p(e, e'\pi^+n)$  measurement. The ratio of these cross sections is

$$R = \frac{\sigma[n(e, e'\pi^-p)]}{\sigma[p(e, e'\pi^+n)]} = \frac{|A_V - A_S|^2}{|A_V + A_S|^2}, \quad (11)$$

where  $A_V$  and  $A_S$  are the isovector and isoscalar amplitudes, respectively. Since the pion pole  $t$ -channel process used for the determination of the pion form factor is purely isovector (owing to  $G$ -parity conservation), the above ratio will be diluted if  $\sigma_T$  is not small or if there are significant non-pole contributions to  $\sigma_L$ . The comparison of the measured  $\pi^-/\pi^+$  ratio with model expectations, therefore, provides an effective means of validating the model used to determine  $\sigma_L$  [183, 184]. The same model, now validated, can likely be used to extract the pion form factor from the  $\sigma_{\text{uns}}$  data.

*5.2.2.  $\pi^+$  form factor projections.* As already discussed above, the value of  $F_\pi(Q^2)$  can be determined by comparing the measured  $\sigma_{\text{uns}}$  at small  $-t$  to the best available electroproduction model, incorporating pion pole and non-pole contributions and validated with  $\pi^-/\pi^+$  data. The model should have the pion form factor as an adjustable parameter, so that the best fit value and its uncertainty at fixed  $(Q^2, W)$  are obtained by comparison of the magnitude and  $t$ -dependences of model and data.

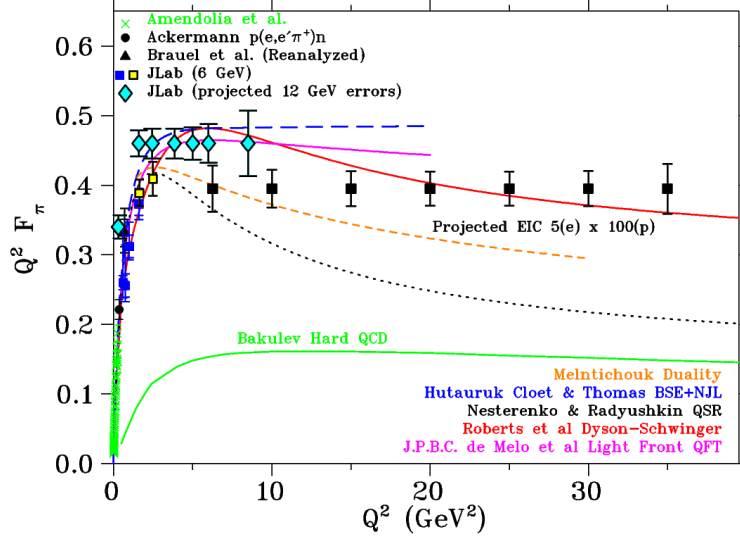


Figure 27: Existing data (green [187, 188]; black [39, 189, 190]; blue and yellow [39, 180, 181]) and projected uncertainties for future data on the pion form factor from JLab (cyan [191]) and EIC (black), in comparison to a variety of hadronic structure calculations (green solid [192]; orange dash [193]; blue long-dash [131]; black dot [194]; red solid [35]; violet solid [195]). The EIC projections clearly cover a much larger  $Q^2$  range than the JLab measurements.

If several models are available, the form factor values obtained with each one can be compared to better understand the model-dependence. The importance of additional  $p(e, e' \pi^+ n)$  model development to improve knowledge of pion form factors cannot be overestimated, and additional activity in this area should be encouraged.

Using this technique, the EIC can enable a pion form factor measurement up to  $Q^2 = 35 \text{ GeV}^2$ , as shown in figure 27. The errors in the yields are based on the following assumptions: cross sections parametrised from the Regge model in [196], integrated luminosity of  $20 \text{ fb}^{-1}$  for  $5 \times 100 \text{ GeV}$  measurement, clean identification of exclusive  $p(e, e' \pi^+ n)$  events by tagging the forward neutron, and a cross section systematic uncertainty of 2.5% point-to-point and 12% scale. One should then apply the following additional uncertainty, since the form factor will be determined from unseparated, rather than L/T-separated data:  $\delta R = R$  systematic uncertainty in the model subtraction to isolate  $\sigma_L$ , where  $R = \sigma_L / \sigma_T = 0.013 - 0.14$  at  $-t_{\min}$ . The model

fitting procedure is finally used to extract  $F_\pi(Q^2)$  from the  $\sigma_{uns}$  data, where one assumes the applied model is validated at small  $-t$  by comparison to data. Additional model uncertainties in the form factor extraction are not estimated here, but the EIC should provide data over a sufficiently large kinematic range to allow the model-dependence to be quantified in a detailed analysis.

*5.2.3.  $K^+$  form factor.* The reliability of the electroproduction method to determine the  $K^+$  form factor is not yet fully established. A recent extraction of the kaon form factor from electroproduction data at  $Q^2 = 1.00, 1.36, 1.90, 2.07, 2.35 \text{ GeV}^2$  is discussed in [197]. The L/T separated kaon electroproduction cross sections were extracted at different values of  $-t$  using data from JLab [180, 198, 199] and the successful method from [180, 182] was applied to determine the kaon form factor. JLab E12-09-011 [42] acquired data for the  $p(e, e'K^+)\Lambda$ ,  $p(e, e'K^+)\Sigma^0$  reactions at hadronic invariant mass  $W = \sqrt{(p_K + p_{\Lambda, \Sigma})^2} > 2.5 \text{ GeV}$ , to search for evidence of scattering from the proton's "kaon cloud". The data are still being analysed, with L/T-separated cross sections expected in the next  $\sim 2$  years.

If the anticipated data confirm that the scattering from the virtual  $K^+$  in the nucleon dominates at low four-momentum transfer to the target  $|t| \ll m_p^2$ , the experiment will yield the world's first quality data for  $F_K$  above  $Q^2 > 0.2 \text{ GeV}^2$ . This would then open up the possibility of using exclusive reactions to determine the  $K^+$  form factor over a wide range of  $Q^2$  at higher energies. While the general technique will remain the same, the  $\pi^-/\pi^+$  validation technique to confirm the  $\sigma_L$  extraction cannot be used for the  $K^+$ . One possibility could be for  $\Lambda/\Sigma^0$  ratios to play a similar role. However, conditions under which the clean separation of these two channels may be possible at the EIC requires further study. These studies are planned for the near future.

## 6. Summary and prospects

After more than seventy years, there is now a growing realisation that the first-ever discovered mesons hold the keys to our further understanding of the vast bulk of visible mass in the Universe. The pion was the first discovered meson, in 1947 [16], soon followed in the same year by the kaon [17], the first strange particle [200, 201]. These Nambu-Goldstone bosons would be massless if Nature expressed chiral symmetry simply; and would remain massless in the absence of quark couplings to a Higgs

boson. Yet, these light pseudoscalar mesons are intimately linked to confinement; their structure is complicated; and their masses, although uncommonly light, are not zero, being generated by constructive interference between an emergent mass mechanism, expressed in dynamical chiral symmetry breaking, and the Higgs mechanism. Some 100 MeV of the 494 MeV kaon mass, with its heavier strange quark, or 20%, may be attributed directly to the Higgs mechanism.

The emergence of the bulk of visible mass and its manifestations in the existence and properties of hadrons and nuclei are profound questions that probe into the heart of strongly interacting matter. What Nature provided as properties of pions and kaons, the Standard Model's would-be Nambu-Goldstone modes, are tell-tales of the emergent hadron mass and structure mechanisms, and the required interplay with the Higgs mechanism. For example, the quark and gluon energy contributions to pion and kaon masses give information on the balance of these mechanisms, the magnitude and scale-dependence of pion and kaon form factors inform about the size and range of the interference between emergent mass and the Higgs-mass mechanisms, the pressure distribution and transverse momentum distributions in pions as compared to protons inform about universality of the attractive and repulsive forces inside hadrons.

Understanding fundamentally requires a synergistic effort that combines experiment, theory, computing, and phenomenology, with the aims being to reveal how the roughly 1 GeV mass-scale that characterises atomic nuclei appears and why it has the observed value; why ground-state pseudoscalar mesons are unnaturally light in comparison; and to elucidate the role of the Higgs boson in forming hadron properties. Pions, kaons, protons and their counterpart neutrons provide the building blocks of the visible universe. Their exact QCD substructures have now readily become available by marked progress in theory and computing, and their further understanding in turn will shed light on how Nature created mass and visible structure.

The foreseen Electron-Ion Collider (EIC) will be a real game changer for experimental data on pion and kaon structure. In specific kinematic regions, an electron scattering process coupled with the observation of recoil nucleons (N) or hyperons (Y) receiving sufficiently low four-momentum transfer,  $-t$ , can reveal features associated with the “meson cloud” of the nucleon. With proper theoretical understanding on the interpretation of the off-shell pion (kaon) target and possible theoretical backgrounds as function of  $-t$ , experimental access to a physical pion (kaon) target is enabled. This can be further experimentally validated by constraining theoretical backgrounds by using both  $ep$  and  $ed$  scattering data, and by ensuring interpretation independent of

$-t$ . Based on present theoretical and experimental guidance, this may be possible for  $-t < 0.6$  (0.9)  $\text{GeV}^2$  for pion (kaon) targets. For elastic scattering, this Sullivan process carries information on the pion or kaon form factor. For deep inelastic scattering, the process informs about the mesonic parton content. Regardless of interpretation, the various tagged pion (kaon) cross section data as a function of  $-t$  are valuable in their own right.

Since only a small fraction of the nucleons emit a virtual meson and only small momentum transfers from the nucleon to the resulting baryon allow the interpretation in terms of a real pion (kaon), the highest luminosities of  $\sim 10^{34}$  electron-nucleons  $\text{cm}^{-2} \text{s}^{-1}$  are necessary. Owing to the long lifetime of the  $\Lambda$ , lower collision (or rather proton/ion beam) energies are slightly favored at the EIC to tag kaon structure. The need to efficiently tag pion and kaon structure is further fundamentally intertwined with the integration of the EIC detector in the interaction region, especially related to any far-forward (in the direction of the proton/ion beam) detection scheme of recoil nucleons and hyperons. All sub-components of the far-forward area play an important role to detect forward-going protons (in Roman pots) and neutrons (in Zero-Degree Calorimeters), and to detect hyperon decay products: protons and negatively charged pions at opposite sides of the beam line, and neutrons and photons originating from neutral pion decays in zero-degree and electromagnetic calorimeters. It is shown that appreciable detection efficiencies are thus achieved, with exception of kaon tagging at the highest EIC proton beam energies (275 GeV). The kaon tagging scheme could be improved by an alternate magneto-optics design, removing a large area with nearby and therefore integrated magnets in the present beam line, and hence no possible detection of decay products, or alternately an improved secondary focus.

This detection scheme allows, through the Sullivan process, excellent prospects for pion (and kaon) structure function measurements over a large range of  $x$  and  $Q^2$ , approaching the vast  $(x, Q^2)$  landscape of the HERA proton structure function measurements. The tagged pion (kaon) cross section data remain precise over a large range of  $-t$ , up to  $-t \sim 0.6 \text{ GeV}^2$  for the pion. This could allow further study of more exclusive semi-inclusive and deeply-virtual Compton scattering data, towards transverse momentum and pressure distributions in the pion. To access the pion form factor, an alternate technique to access the longitudinal cross section is used, via a model, validated with exclusive  $\pi^+/\pi^-$  ratios from deuterium. Scattering from the pion cloud dominates the longitudinal cross section at low  $-t$ , and, if dominant, this ratio would approach unity. This could allow precise pion form factor determination at

EIC up to  $Q^2 \sim 35 \text{ GeV}^2$ . The reliability of a similar  $\Lambda/\Sigma$  ratio method to extract the kaon form factor has not yet been established, but it may be studied from a Jefferson Lab 12-GeV kaon electroproduction experiment that ran in 2018/2019.

The EIC will play a key role to access pion and kaon structure over a wide range of centre-of-mass (CM) energies,  $\sim 2 - 140 \text{ GeV}$ , to chart in-pion and in-kaon distributions of mass, charge, magnetisation, and perhaps angular momentum. Nonetheless, to provide experimental measurements guiding theoretical understanding requires a coherent, worldwide effort. Jefferson Lab will provide, at its CM energy  $\sim 5 \text{ GeV}$ , data for the pion (kaon) form factor up to  $Q^2 \sim 10(5) \text{ GeV}^2$  and for insights into mechanisms competing with the Sullivan process, and early measurements of the pion (kaon) structure functions at large- $x$  ( $> 0.5$ ). AMBER can provide pion, and especially much-needed kaon, Drell-Yan measurements in the CM energy region  $\sim 10 - 20 \text{ GeV}$ . These measurements are critical elements in a global effort on pion and kaon structure function measurements. They also allow an independent determination of the “pion flux” for EIC Sullivan process measurements. An Electron-Ion Collider in China (EicC) is under consideration, with CM energy  $\sim 10 - 20 \text{ GeV}$  perfectly attuned to AMBER and forming a bridge from Jefferson Lab to EIC.

Successful completion of the programme sketched herein will deliver deep, far-reaching insights into the distributions and apportionment of charge, mass, and spin within the pion and kaon; the similarities and differences between such distributions in these (almost) Nambu-Goldstone modes and the benchmark proton; the symbiotic relationship between the emergence of hadron mass and confinement; and the character and consequences of constructive interference between the Standard Model’s two mass-generating mechanisms. It has the potential to finally complete a chapter in science whose first lines were written more than eighty years ago and contained the prediction of the pion’s existence [202].

## Acknowledgments

This work was supported in part by the U.S. Department of Energy, Office of Science, Office of Nuclear Physics, under contracts DE-AC05-06OR23177, DE-FG02-03ER41260; the US National Science Foundation under grants PHY-1653405, PHY-1714133, PHY-2012430; the Natural Sciences and Engineering Research Council of Canada (NSERC), FRN: SAPIN-2016-00031; the Jiangsu Province *Hundred Talents Plan for Professionals*; Ministerio Español de Ciencia e Innovación, grant no. PID2019-



107844GB-C22; Junta de Andalucía, contract nos. P18-FRJ-1132; Operativo FEDER Andalucía 2014-2020 UHU-1264517; Conselho Nacional de Desenvolvimento Científico e Tecnológico (CNPq) under grant no. 308486/2015-3; Fundação de Amparo à Pesquisa do Estado de São Paulo (FAPESP) under the thematic project grant 2017/05660-0; INCT-FNA project 464898/2014-5; Coordenação de Aperfeiçoamento de Pessoal de Nível Superior (CAPES—Finance Code 001); Research Corporation for Science Advancement through the Cottrell Scholar Award. The work of NS was supported by the DOE, Office of Science, Office of Nuclear Physics in the Early Career Program. Contributions of and discussions with Wally Melnitchouk are gratefully acknowledged. The authors would like to thank Wim Cosyn and Doug Higinbotham for helpful comments during this work and preparation of this manuscript. The authors would also like to thank Zafar Ahmed, Rory Evans and Wenliang (Bill) Li for their work and assistance on the DEMP event generator.

## References

- [1] Peter W. Higgs. Broken Symmetries and the Masses of Gauge Bosons. *Phys. Rev. Lett.*, 13:508–509, 1964.
- [2] Georges Aad et al. Observation of a new particle in the search for the Standard Model Higgs boson with the ATLAS detector at the LHC. *Phys. Lett. B*, 716:1–29, 2012.
- [3] Serguei Chatrchyan et al. Observation of a New Boson at a Mass of 125 GeV with the CMS Experiment at the LHC. *Phys. Lett. B*, 716:30–61, 2012.
- [4] Craig D. Roberts and Sebastian M. Schmidt. Reflections upon the Emergence of Hadronic Mass. *Eur. Phys. J. ST*, 229(22-23):3319–3340, 2020.
- [5] Craig D Roberts. Empirical Consequences of Emergent Mass. *Symmetry*, 12(9):1468, 2020.
- [6] Craig D. Roberts. On Mass and Matter – arXiv:2101.08340 [hep-ph]. *AAPPS Bulletin*, page *in press*, 1 2021.
- [7] P. Pascual and R. Tarrach. *QCD: Renormalization for the Practitioner*. Springer-Verlag, Berlin, 1984. Lecture Notes in Physics **194**.
- [8] Jacobo Ruiz de Elvira, Martin Hoferichter, Bastian Kubis, and Ulf-G. Meißner. Extracting the  $\sigma$ -term from low-energy pion-nucleon scattering. *J. Phys. G*, 45(2):024001, 2018.

- [9] P. A. Zyla et al. Review of particle properties. *Prog. Theor. Exp. Phys.*, 083C01, 2020.
- [10] Yoichiro Nambu. Quasiparticles and Gauge Invariance in the Theory of Superconductivity. *Phys. Rev.*, 117:648–663, 1960.
- [11] J. Goldstone. Field Theories with Superconductor Solutions. *Nuovo Cim.*, 19:154–164, 1961.
- [12] Xiang-Dong Ji. Breakup of hadron masses and energy - momentum tensor of QCD. *Phys. Rev. D*, 52:271–281, 1995.
- [13] Arlene C. Aguilar et al. Pion and Kaon Structure at the Electron-Ion Collider. *Eur. Phys. J. A*, 55(10):190, 2019.
- [14] S. J. Brodsky et al. Strong QCD from Hadron Structure Experiments – arXiv:2006.06802 [hep-ph]. *Intern. J. Mod. Phys. E*, page in press, 6 2020.
- [15] Toni Feder. Brookhaven facility to be transformed into electron-ion collider. *Physics Today*, 73:22, 2020.
- [16] C. M. G. Lattes, H. Muirhead, G. P. S. Occhialini, and C. F. Powell. Processes involving charged mesons. *Nature*, 159:694–697, 1947.
- [17] G. D. Rochester and C. C. Butler. Evidence for the Existence of New Unstable Elementary Particles. *Nature*, 160:855–857, 1947.
- [18] G. Peter Lepage and Stanley J. Brodsky. Exclusive Processes in Quantum Chromodynamics: Evolution Equations for Hadronic Wave Functions and the Form-Factors of Mesons. *Phys. Lett. B*, 87:359–365, 1979.
- [19] A.V. Efremov and A.V. Radyushkin. Factorization and Asymptotical Behavior of Pion Form-Factor in QCD. *Phys. Lett. B*, 94:245–250, 1980.
- [20] Glennys R. Farrar and Darrell R. Jackson. The Pion Form-Factor. *Phys. Rev. Lett.*, 43:246, 1979.
- [21] G. Peter Lepage and Stanley J. Brodsky. Exclusive Processes in Perturbative Quantum Chromodynamics. *Phys. Rev. D*, 22:2157, 1980.
- [22] Craig D. Roberts. Three Lectures on Hadron Physics. *J. Phys. Conf. Ser.*, 706:022003, 2016. arXiv:1509.02925 [nucl-th].
- [23] Tanja Horn and Craig D. Roberts. The pion: an enigma within the Standard Model. *J. Phys. G.*, 43:073001, 2016.

- [24] Gernot Eichmann, Helios Sanchis-Alepuz, Richard Williams, Reinhard Alkofer, and Christian S. Fischer. Baryons as relativistic three-quark bound states. *Prog. Part. Nucl. Phys.*, 91:1–100, 2016.
- [25] Volker D. Burkert and Craig D. Roberts. Roper resonance: Toward a solution to the fifty year puzzle. *Rev. Mod. Phys.*, 91:011003, 2019. arXiv:1710.02549 [nucl-ex].
- [26] Si-Xue Qin and C. D. Roberts. Impressions of the continuum bound state problem in QCD. *Chinese Physics Letters*, 37(12):121201, dec 2020.
- [27] J.H.O. Sales, T. Frederico, B.V. Carlson, and P.U. Sauer. Light front Bethe-Salpeter equation. *Phys. Rev. C*, 61:044003, 2000.
- [28] T. Frederico, E. Pace, B. Pasquini, and G. Salme. Pion Generalized Parton Distributions with covariant and Light-front constituent quark models. *Phys. Rev. D*, 80:054021, 2009.
- [29] J. Carbonell and V.A. Karmanov. Solving Bethe-Salpeter equation for two fermions in Minkowski space. *Eur. Phys. J. A*, 46:387–397, 2010.
- [30] Giovanni Salme, Tobias Frederico, and Michele Viviani. Solutions of the Bethe-Salpeter Equation in Minkowski space: a comparative study. *Few Body Syst.*, 55:693–696, 2014.
- [31] Giovanni Salme. Investigating the homogeneous Bethe-Salpeter equation in Minkowski space. *J. Phys. Conf. Ser.*, 527:012026, 2014.
- [32] W. de Paula, T. Frederico, G. Salmè, and M. Viviani. Advances in solving the two-fermion homogeneous Bethe-Salpeter equation in Minkowski space. *Phys. Rev. D*, 94(7):071901, 2016.
- [33] Lei Chang, I.C. Cloet, J.J. Cobos-Martinez, C.D. Roberts, S.M. Schmidt, and P.C. Tandy. Imaging dynamical chiral symmetry breaking: pion wave function on the light front. *Phys. Rev. Lett.*, 110(13):132001, 2013.
- [34] Gerard 't Hooft. A Two-Dimensional Model for Mesons. *Nucl. Phys. B*, 75:461–470, 1974.
- [35] L. Chang, I.C. Cloet, C.D. Roberts, S.M. Schmidt, and P.C. Tandy. Pion electromagnetic form factor at spacelike momenta. *Phys. Rev. Lett.*, 111(14):141802, 2013.

- [36] Muyang Chen, Minghui Ding, Lei Chang, and Craig D. Roberts. Mass-dependence of pseudoscalar meson elastic form factors. *Phys. Rev. D*, 98(9):091505, 2018.
- [37] Fei Gao, Lei Chang, Yu-Xin Liu, Craig D. Roberts, and Peter C. Tandy. Exposing strangeness: projections for kaon electromagnetic form factors. *Phys. Rev. D*, 96(3):034024, 2017.
- [38] T. Horn et al. Scaling study of the pion electroproduction cross sections and the pion form factor. *Phys. Rev. C*, 78:058201, 2008.
- [39] G.M. Huber et al. Charged pion form-factor between  $Q^2 = 0.60 \text{ GeV}^2$  and  $2.45 \text{ GeV}^2$ . II. Determination of, and results for, the pion form-factor. *Phys. Rev. C*, 78:045203, 2008.
- [40] G. M. Huber, D. Gaskell, et al. Measurement of the Charged Pion Form Factor to High  $Q^2$ . Jefferson Lab Experiment E12-06-101.
- [41] T. Horn, G. M. Huber, et al. Scaling Study of the L/T-Separated Pion Electroproduction Cross Section at 11 GeV. Jefferson Lab 12 GeV Experiment E12-07-105.
- [42] T. Horn, G. M. Huber, P. Markowitz, et al. Studies of the L/T Separated Kaon Electroproduction Cross Sections from 5-11 GeV. Jefferson Lab 12 GeV Experiment E12-09-011.
- [43] Si-Xue Qin, Chen Chen, Cedric Mezrag, and Craig D. Roberts. Off-shell persistence of composite pions and kaons. *Phys. Rev. C*, 97(1):015203, 2018.
- [44] Ho-Meoyng Choi, T. Frederico, Chueng-Ryong Ji, and J.P.B.C. de Melo. Pion off-shell electromagnetic form factors: data extraction and model analysis. *Phys. Rev. D*, 100(11):116020, 2019.
- [45] R.Keith Ellis, W.James Stirling, and B.R. Webber. *QCD and collider physics*, volume 8. Cambridge University Press, 2 2011.
- [46] Kenneth D. Lane. Asymptotic Freedom and Goldstone Realization of Chiral Symmetry. *Phys. Rev. D*, 10:2605, 1974.
- [47] H. David Politzer. Effective Quark Masses in the Chiral Limit. *Nucl. Phys. B*, 117:397, 1976.
- [48] Pieter Maris, Craig D. Roberts, and Peter C. Tandy. Pion mass and decay constant. *Phys. Lett. B*, 420:267–273, 1998.

- [49] Z.F. Ezawa. Wide-Angle Scattering in Softened Field Theory. *Nuovo Cim. A*, 23:271–290, 1974.
- [50] Glennys R. Farrar and Darrell R. Jackson. Pion and Nucleon Structure Functions Near  $x=1$ . *Phys. Rev. Lett.*, 35:1416, 1975.
- [51] Edmond L. Berger and Stanley J. Brodsky. Quark Structure Functions of Mesons and the Drell-Yan Process. *Phys. Rev. Lett.*, 42:940–944, 1979.
- [52] Stanley J. Brodsky, Matthias Burkardt, and Ivan Schmidt. Perturbative QCD constraints on the shape of polarized quark and gluon distributions. *Nucl. Phys. B*, 441:197–214, 1995.
- [53] Feng Yuan. Generalized parton distributions at  $x \rightarrow 1$ . *Phys. Rev. D*, 69:051501, 2004.
- [54] Yuri L. Dokshitzer. Calculation of the Structure Functions for Deep Inelastic Scattering and  $e^+ e^-$  Annihilation by Perturbation Theory in Quantum Chromodynamics. *Sov. Phys. JETP*, 46:641–653, 1977.
- [55] V.N. Gribov and L.N. Lipatov. Deep inelastic electron scattering in perturbation theory. *Phys. Lett. B*, 37:78–80, 1971.
- [56] L.N. Lipatov. The parton model and perturbation theory. *Sov. J. Nucl. Phys.*, 20:94–102, 1975.
- [57] Guido Altarelli and G. Parisi. Asymptotic Freedom in Parton Language. *Nucl. Phys. B*, 126:298–318, 1977.
- [58] Richard D. Ball, Emanuele R. Nocera, and Juan Rojo. The asymptotic behaviour of parton distributions at small and large  $x$ . *Eur. Phys. J. C*, 76(7):383, 2016.
- [59] S.D. Drell and Tung-Mow Yan. Connection of Elastic Electromagnetic Nucleon Form-Factors at Large  $Q^2$  and Deep Inelastic Structure Functions Near Threshold. *Phys. Rev. Lett.*, 24:181–185, 1970.
- [60] Geoffrey B. West. Phenomenological model for the electromagnetic structure of the proton. *Phys. Rev. Lett.*, 24:1206–1209, 1970.
- [61] Z.F. Ezawa. Drell-Yan-West relation for deep inelastic and elastic form-factors. *Nucl. Phys. B*, 58:295–300, 1973.
- [62] P.V. Landshoff and J.C. Polkinghorne. Threshold properties of electroproduction and annihilation. *Nucl. Phys. B*, 53:473–483, 1973.
- [63] J. Badier et al. Experimental Determination of the pi Meson Structure Functions by the Drell-Yan Mechanism. *Z. Phys. C*, 18:281, 1983.

- [64] J.S. Conway et al. Experimental Study of Muon Pairs Produced by 252-GeV Pions on Tungsten. *Phys. Rev. D*, 39:92–122, 1989.
- [65] P.C. Barry, N. Sato, W. Melnitchouk, and Chueng-Ryong Ji. First Monte Carlo Global QCD Analysis of Pion Parton Distributions. *Phys. Rev. Lett.*, 121(15):152001, 2018.
- [66] Ivan Novikov et al. Parton Distribution Functions of the Charged Pion Within The xFitter Framework. *Phys. Rev. D*, 102(1):014040, 2020.
- [67] Chengdong Han, Gang Xie, Rong Wang, and Xurong Chen. An Analysis of Parton Distribution Functions of the Pion and the Kaon with the Maximum Entropy Input. arXiv:2010.14284 [hep-ph], 2020.
- [68] Matthias Aicher, Andreas Schafer, and Werner Vogelsang. Soft-gluon resummation and the valence parton distribution function of the pion. *Phys. Rev. Lett.*, 105:252003, 2010.
- [69] P.C. Barry, Chueng-Ryong Ji, W. Melnitchouk, and N. Sato. Threshold resummation effects on pion PDFs at large  $x$ . (in preparation).
- [70] Z.-F Cui, M. Ding, F. Gao, Daniele Binosi, Lei Chang, C. Roberts, J. Rodríguez-Quintero, and S. Schmidt. Higgs modulation of emergent mass as revealed in kaon and pion parton distributions. *The European Physical Journal A*, 57, 01 2021.
- [71] Zhu-Fang Cui, Minghui Ding, Fei Gao, Khépani Raya, Daniele Binosi, Lei Chang, Craig D Roberts, Jose Rodríguez-Quintero, and Sebastian M Schmidt. Kaon and pion parton distributions. *Eur. Phys. J. C*, 80(11):1064, 2020.
- [72] Raza Sabbir Sufian, Joseph Karpie, Colin Egerer, Kostas Orginos, Jian-Wei Qiu, and David G. Richards. Pion Valence Quark Distribution from Matrix Element Calculated in Lattice QCD. *Phys. Rev. D*, 99(7):074507, 2019.
- [73] Jian-Hui Zhang, Jiunn-Wei Chen, Luchang Jin, Huey-Wen Lin, Andreas Schäfer, and Yong Zhao. First direct lattice-QCD calculation of the  $x$ -dependence of the pion parton distribution function. *Phys. Rev. D*, 100(3):034505, 2019.
- [74] M.B. Hecht, Craig D. Roberts, and S.M. Schmidt. Valence quark distributions in the pion. *Phys. Rev. C*, 63:025213, 2001.
- [75] Huey-Wen Lin, Jiunn-Wei Chen, Zhouyou Fan, Jian-Hui Zhang, and Rui Zhang. The Valence-Quark Distribution of the Kaon from Lattice QCD. *Phys. Rev. D*, 103(1):014516, 2021.

- [76] J. Badier et al. Measurement of the  $K^-/\pi^-$  Structure Function Ratio Using the Drell-Yan Process. *Phys. Lett. B*, 93:354–356, 1980.
- [77] Minghui Ding et al. Drawing insights from pion parton distributions. *Chin. Phys. C (Lett.)*, 44:031002, 2020.
- [78] Minghui Ding, Khépani Raya, Daniele Binosi, Lei Chang, Craig D Roberts, and Sebastian M. Schmidt. Symmetry, symmetry breaking, and pion parton distributions. *Phys. Rev. D*, 101(5):054014, 2020.
- [79] W. de Paula, E. Ydrefors, J. Alvarenga Nogueira, Tobias Frederico, and Giovanni Salmè. The pion valence momentum distributions and 3D image with Minkowski space dynamics. *in preparation*, 2020.
- [80] Jin-Li Zhang, Zhu-Fang Cui, Jialun Ping, and Craig D Roberts. Contact interaction analysis of pion GTMDs. *Eur. Phys. J. C*, 81(1):6, 2021.
- [81] D. Brömmel et al. The Spin structure of the pion. *Phys. Rev. Lett.*, 101:122001, 2008.
- [82] Seung-il Nam and Hyun-Chul Kim. Spin structure of the pion from the instanton vacuum. *Phys. Lett. B*, 700:305–312, 2011.
- [83] Alexander E. Dorokhov, Wojciech Broniowski, and Enrique Ruiz Arriola. Generalized Quark Transversity Distribution of the Pion in Chiral Quark Models. *Phys. Rev. D*, 84:074015, 2011.
- [84] Cristiano Fanelli, Emanuele Pace, Giovanni Romanelli, Giovanni Salme, and Marco Salmistraro. Pion Generalized Parton Distributions within a fully covariant constituent quark model. *Eur. Phys. J. C*, 76:253, 2016.
- [85] Jin-Li Zhang, Khépani Raya, Lei Chang, Zhu-Fang Cui, José Manuel Morgado, Craig D. Roberts, and José Rodríguez-Quintero. Measures of pion and kaon structure from generalised parton distributions. arXiv:2101.12286 [hep-ph], 2021.
- [86] Kenneth G. Wilson. Confinement of quarks. *Phys. Rev. D*, 10:2445–2459, 1974.
- [87] Keh-Fei Liu and Shao-Jing Dong. Origin of difference between anti-d and anti-u partons in the nucleon. *Phys. Rev. Lett.*, 72:1790–1793, 1994.
- [88] K.F. Liu, S.J. Dong, Terrence Draper, D. Leinweber, J.H. Sloan, W. Wilcox, and R.M. Woloshyn. Valence QCD: Connecting QCD to the quark model. *Phys. Rev. D*, 59:112001, 1999.
- [89] Keh-Fei Liu. Parton degrees of freedom from the path integral formalism. *Phys. Rev. D*, 62:074501, 2000.

- [90] William Detmold and C.J.David Lin. Deep-inelastic scattering and the operator product expansion in lattice QCD. *Phys. Rev. D*, 73:014501, 2006.
- [91] V. Braun and Dieter Müller. Exclusive processes in position space and the pion distribution amplitude. *Eur. Phys. J. C*, 55:349–361, 2008.
- [92] Xiangdong Ji. Parton Physics on a Euclidean Lattice. *Phys. Rev. Lett.*, 110:262002, 2013.
- [93] Xiangdong Ji. Parton Physics from Large-Momentum Effective Field Theory. *Sci. China Phys. Mech. Astron.*, 57:1407–1412, 2014.
- [94] Xiangdong Ji, Yu-Sheng Liu, Yizhuang Liu, Jian-Hui Zhang, and Yong Zhao. Large-Momentum Effective Theory. arXiv:2004.03543 [hep-ph], 2020.
- [95] Anatoly Radyushkin. Nonperturbative Evolution of Parton Quasi-Distributions. *Phys. Lett. B*, 767:314–320, 2017.
- [96] A.J. Chambers, R. Horsley, Y. Nakamura, H. Perlt, P.E.L. Rakow, G. Schierholz, A. Schiller, K. Somfleth, R.D. Young, and J.M. Zanotti. Nucleon Structure Functions from Operator Product Expansion on the Lattice. *Phys. Rev. Lett.*, 118(24):242001, 2017.
- [97] Yan-Qing Ma and Jian-Wei Qiu. Extracting Parton Distribution Functions from Lattice QCD Calculations. *Phys. Rev. D*, 98(7):074021, 2018.
- [98] Yan-Qing Ma and Jian-Wei Qiu. QCD Factorization and PDFs from Lattice QCD Calculation. *Int. J. Mod. Phys. Conf. Ser.*, 37:1560041, 2015.
- [99] Yan-Qing Ma and Jian-Wei Qiu. Exploring Partonic Structure of Hadrons Using ab initio Lattice QCD Calculations. *Phys. Rev. Lett.*, 120(2):022003, 2018.
- [100] Huey-Wen Lin et al. Parton distributions and lattice QCD calculations: a community white paper. *Prog. Part. Nucl. Phys.*, 100:107–160, 2018.
- [101] Krzysztof Cichy and Martha Constantinou. A guide to light-cone PDFs from Lattice QCD: an overview of approaches, techniques and results. *Adv. High Energy Phys.*, 2019:3036904, 2019.
- [102] Rui Zhang, Carson Honkala, Huey-Wen Lin, and Jiunn-Wei Chen. Pion and kaon distribution amplitudes in the continuum limit. *Phys. Rev. D*, 102(9):094519, 2020.
- [103] Gunnar S. Bali et al. Pion distribution amplitude from Euclidean correlation functions. *Eur. Phys. J. C*, 78(3):217, 2018.



- [104] Gunnar S. Bali, Vladimir M. Braun, Benjamin Glässle, Meinulf Göckeler, Michael Gruber, Fabian Hutzler, Piotr Korcyl, Andreas Schäfer, Philipp Wein, and Jian-Hui Zhang. Pion distribution amplitude from Euclidean correlation functions: Exploring universality and higher-twist effects. *Phys. Rev. D*, 98(9):094507, 2018.
- [105] Craig D Roberts. Insights into the Origin of Mass. In *27th International Nuclear Physics Conference*, 9 2019.
- [106] Taku Izubuchi, Luchang Jin, Christos Kallidonis, Nikhil Karthik, Swagato Mukherjee, Peter Petreczky, Charles Shugert, and Sergey Syritsyn. Valence parton distribution function of pion from fine lattice. *Phys. Rev. D*, 100(3):034516, 2019.
- [107] Bálint Joó, Joseph Karpie, Kostas Orginos, Anatoly V. Radyushkin, David G. Richards, Raza Sabbir Sufian, and Savvas Zafeiropoulos. Pion valence structure from Ioffe-time parton pseudodistribution functions. *Phys. Rev. D*, 100(11):114512, 2019.
- [108] Raza Sabbir Sufian, Colin Egerer, Joseph Karpie, Robert G. Edwards, Bálint Joó, Yan-Qing Ma, Kostas Orginos, Jian-Wei Qiu, and David G. Richards. Pion Valence Quark Distribution from Current-Current Correlation in Lattice QCD. *Phys. Rev. D*, 102(5):054508, 2020.
- [109] Jiunn-Wei Chen, Huey-Wen Lin, and Jian-Hui Zhang. Pion generalized parton distribution from lattice QCD. *Nucl. Phys. B*, 952:114940, 2020.
- [110] Zhou-You Fan, Yi-Bo Yang, Adam Anthony, Huey-Wen Lin, and Keh-Fei Liu. Gluon Quasi-Parton-Distribution Functions from Lattice QCD. *Phys. Rev. Lett.*, 121(24):242001, 2018.
- [111] Ian Balitsky, Wayne Morris, and Anatoly Radyushkin. Gluon Pseudo-Distributions at Short Distances: Forward Case. *Phys. Lett. B*, 808:135621, 2020.
- [112] Wei Wang, Jian-Hui Zhang, Shuai Zhao, and Ruilin Zhu. Complete matching for quasidistribution functions in large momentum effective theory. *Phys. Rev. D*, 100(7):074509, 2019.
- [113] Jian-Hui Zhang, Xiangdong Ji, Andreas Schäfer, Wei Wang, and Shuai Zhao. Accessing Gluon Parton Distributions in Large Momentum Effective Theory. *Phys. Rev. Lett.*, 122(14):142001, 2019.

- [114] Zhouyou Fan, Rui Zhang, and Huey-Wen Lin. Nucleon Gluon Distribution Function from 2+1+1-Flavor Lattice QCD, 2020. arXiv:2007.16113 [hep-lat].
- [115] Matthias Burkardt. Impact parameter space interpretation for generalized parton distributions. *Int. J. Mod. Phys. A*, 18:173–208, 2003.
- [116] M. Diehl. Generalized parton distributions. *Phys. Rept.*, 388:41–277, 2003.
- [117] John C. Collins, Davison E. Soper, and George F. Sterman. *Factorization of Hard Processes in QCD*, volume 5, pages 1–91. 1989.
- [118] J.F. Owens.  $Q^2$ -dependent parametrizations of pion parton distribution functions. *Phys. Rev. D*, 30:943, 1984.
- [119] P. Aurenche, R. Baier, M. Fontannaz, M.N. Kienzle-Focacci, and M. Werlen. The Gluon Content of the Pion From High  $p_T$  Direct Photon Production. *Phys. Lett. B*, 233:517–521, 1989.
- [120] P.J. Sutton, Alan D. Martin, R.G. Roberts, and W.James Stirling. Parton distributions for the pion extracted from Drell-Yan and prompt photon experiments. *Phys. Rev. D*, 45:2349–2359, 1992.
- [121] M. Gluck, E. Reya, and A. Vogt. Pionic parton distributions. *Z. Phys. C*, 53:651–656, 1992.
- [122] M. Glück, E. Reya, and I. Schienbein. Pionic parton distributions revisited. *Eur. Phys. J. C*, 10:313–317, 1999.
- [123] K. Wijesooriya, P.E. Reimer, and R.J. Holt. The pion parton distribution function in the valence region. *Phys. Rev. C*, 72:065203, 2005.
- [124] B. Betev et al. Differential Cross-section of high mass muon pairs produced by a 194 GeV/c  $\pi^-$  beam on a tungsten target. *Z. Phys. C*, 28:9, 1985.
- [125] J.S. Conway et al. Experimental Study of Muon Pairs Produced by 252-GeV Pions on Tungsten. *Phys. Rev. D*, 39:92–122, 1989.
- [126] S. Chekanov et al. Leading neutron production in  $e^+ p$  collisions at HERA. *Nucl. Phys. B*, 637:3–56, 2002.
- [127] F.D. Aaron et al. Measurement of Leading Neutron Production in Deep-Inelastic Scattering at HERA. *Eur. Phys. J. C*, 68:381–399, 2010.
- [128] J.R. McKenney, Nobuo Sato, W. Melnitchouk, and Chueng-Ryong Ji. Pion structure function from leading neutron electroproduction and SU(2) flavor asymmetry. *Phys. Rev. D*, 93(5):054011, 2016.

- [129] Roy J. Holt and Craig D. Roberts. Distribution Functions of the Nucleon and Pion in the Valence Region. *Rev. Mod. Phys.*, 82:2991–3044, 2010.
- [130] Santiago Noguera and Sergio Scopetta. Pion transverse momentum dependent parton distributions in the nambu and jona-lasinio model. *JHEP*, 11:102, 2015.
- [131] Parada T. P. Hutaeruk, Ian C. Cloet, and Anthony W. Thomas. Flavor dependence of the pion and kaon form factors and parton distribution functions. *Phys. Rev. C*, 94(3):035201, 2016.
- [132] T.J. Hobbs. Quantifying finite-momentum effects in the quark quasidistribution functions of mesons. *Phys. Rev. D*, 97(5):054028, 2018.
- [133] Shu-Sheng Xu, Lei Chang, Craig D. Roberts, and Hong-Shi Zong. Pion and kaon valence-quark parton quasidistributions. *Phys. Rev. D*, 97(9):094014, 2018.
- [134] Jiangshan Lan, Chandan Mondal, Shaoyang Jia, Xingbo Zhao, and James P. Vary. Parton Distribution Functions from a Light Front Hamiltonian and QCD Evolution for Light Mesons. *Phys. Rev. Lett.*, 122:172001, May 2019.
- [135] Lei Chang, Khépani Raya, and Xiaobin Wang. Pion Parton Distribution Function in Light-Front Holographic QCD. *Chin. Phys. C*, 44(11):114105, 2020.
- [136] Arthur Kock, Yizhuang Liu, and Ismail Zahed. Pion and kaon parton distributions in the QCD instanton vacuum. *Phys. Rev. D*, 102(1):014039, 2020.
- [137] Matthias Aicher, Andreas Schafer, and Werner Vogelsang. Threshold-Resummed Cross Section for the Drell-Yan Process in Pion-Nucleon Collisions at COMPASS. *Phys. Rev. D*, 83:114023, 2011.
- [138] Marco Bonvini, Simone Marzani, Juan Rojo, Luca Rottoli, Maria Ubiali, Richard D. Ball, Valerio Bertone, Stefano Carrazza, and Nathan P. Hartland. Parton distributions with threshold resummation. *JHEP*, 09:191, 2015.
- [139] David Westmark and J.F. Owens. Enhanced threshold resummation formalism for lepton pair production and its effects in the determination of parton distribution functions. *Phys. Rev. D*, 95(5):056024, 2017.
- [140] Werner Vogelsang. Soft-gluon resummation and the pion parton distribution function, June 2020. 06.02-05, CFNS Workshop Series: *Pion and Kaon Structure Functions at the EIC*.
- [141] D. Adikaram et al. Measurement of Tagged Deep Inelastic Scattering (TDIS). Jefferson Lab experiment E12-15-006.

- [142] T.J. Hobbs. Phenomenological Implications of the Nucleon's Meson Cloud. *Few Body Syst.*, 56(6-9):363–368, 2015.
- [143] J. Annand et al. Measurement of Kaon Structure Function through Tagged Deep Inelastic Scattering (TDIS). Jefferson Lab experiment C12-15-006A.
- [144] Nina Cao, P.C. Barry, N. Sato, and W. Melnitchouk. Towards the 3-dimensional parton structure of the pion: integrating transverse momentum data into global QCD analysis. (in preparation).
- [145] Yi-Bo Yang, Ying Chen, Terrence Draper, Ming Gong, Keh-Fei Liu, Zhaofeng Liu, and Jian-Ping Ma. Meson Mass Decomposition from Lattice QCD. *Phys. Rev. D*, 91(7):074516, 2015.
- [146] A.V. Radyushkin. Quasi-parton distribution functions, momentum distributions, and pseudo-parton distribution functions. *Phys. Rev. D*, 96(3):034025, 2017.
- [147] Joseph Karpie, Kostas Orginos, Alexander Rothkopf, and Savvas Zafeiropoulos. Reconstructing parton distribution functions from Ioffe time data: from Bayesian methods to Neural Networks. *JHEP*, 04:057, 2019.
- [148] Luigi Del Debbio, Tommaso Giani, Joseph Karpie, Kostas Orginos, Anatoly Radyushkin, and Savvas Zafeiropoulos. Neural-network analysis of Parton Distribution Functions from Ioffe-time pseudodistributions. arXiv:2010.03996 [hep-ph], 2020.
- [149] Martha Constantinou et al. Parton distributions and lattice QCD calculations: toward 3D structure. arXiv:2006.08636 [hep-ph], 2020.
- [150] J. Bringewatt, N. Sato, W. Melnitchouk, Jian-Wei Qiu, F. Steffens, and M. Constantinou. Confronting lattice parton distributions with global QCD analysis. *Phys. Rev. D*, 103:016003, Jan 2021.
- [151] Huey-Wen Lin, W. Melnitchouk, Alexei Prokudin, N. Sato, and H. Shows. First Monte Carlo Global Analysis of Nucleon Transversity with Lattice QCD Constraints. *Phys. Rev. Lett.*, 120(15):152502, 2018.
- [152] Constantia Alexandrou, Krzysztof Cichy, Martha Constantinou, Kyriakos Hadjiyiannakou, Karl Jansen, Aurora Scapellato, and Fernanda Steffens. Unpolarized and helicity generalized parton distributions of the proton within lattice QCD. *Phys. Rev. Lett.*, 125(26):262001, 2020.
- [153] Huey-Wen Lin. Nucleon Tomography and Generalized Parton Distribution at Physical Pion Mass from Lattice QCD. 2020. arXiv:2008.12474 [hep-ph].

- [154] Anatoly V. Radyushkin. Generalized parton distributions and pseudodistributions. *Phys. Rev. D*, 100(11):116011, 2019.
- [155] T.J. Hobbs, Bo-Ting Wang, Pavel M. Nadolsky, and Fredrick I. Olness. Charting the coming synergy between lattice QCD and high-energy phenomenology. *Phys. Rev. D*, 100(9):094040, 2019.
- [156] Karol Kovařík, Pavel M. Nadolsky, and Davison E. Soper. Hadronic structure in high-energy collisions. *Rev. Mod. Phys.*, 92:045003, Nov 2020.
- [157] P. A. M. Dirac. Forms of relativistic dynamics. *Rev. Mod. Phys.*, 21:392–399, Jul 1949.
- [158] Gerald A. Miller and Stanley J. Brodsky. Frame-independent spatial coordinate  $\tilde{z}$ : Implications for light-front wave functions, deep inelastic scattering, light-front holography, and lattice qcd calculations. *Phys. Rev. C*, 102:022201, Aug 2020.
- [159] W. de Paula, E. Ydrefors, J. H. Alvarenga Nogueira, T. Frederico, and G. Salmè. Observing the minkowskian dynamics of the pion on the null-plane. *Phys. Rev. D*, 103:014002, Jan 2021.
- [160] S. J. Brodsky, V. D. Burkert, D. S. Carman, J. P. Chen, Z.-F. Cui, M. Döring, H. G. Dosch, J. Draayer, L. Elouadrhiri, D. I. Glazier, A. N. Hiller Blin, T. Horn, K. Joo, H. C. Kim, V. Kubarovsky, S. E. Kuhn, Y. Lu, W. Melnitchouk, C. Mezrag, V.I. Mokeev, J. W. Qiu, M. Radici, D. Richards, C. D. Roberts, J. Rodríguez-Quintero, J. Segovia, A. P. Szczepaniak, G. F. de Téramond, and D. Winney. Strong QCD from Hadron Structure Experiments. *International Journal of Modern Physics E*, 29(08):2030006, 2020.
- [161] J.P.B.C. de Melo, J.H.O. Sales, T. Frederico, and P.U. Sauer. Pairs in the light-front and covariance. *Nuclear Physics A*, 631:574–579, Mar 1998.
- [162] John Collins. The non-triviality of the vacuum in light-front quantization: An elementary treatment, 2018.
- [163] Sophia S. Chabysheva and John R. Hiller. Transitioning from equal-time to light-front quantization in  $\phi_2^4$  theory. *Phys. Rev. D*, 102:116010, Dec 2020.
- [164] Lubomir Martinovic and Alexander Dorokhov. Vacuum loops in light-front field theory. *Phys. Lett. B*, 811:135925, 2020.
- [165] Philip D. Mannheim, Peter Lowdon, and Stanley J. Brodsky. Comparing light-front quantization with instant-time quantization, 2020.

- [166] J.D. Sullivan. One pion exchange and deep inelastic electron - nucleon scattering. *Phys. Rev. D*, 5:1732–1737, 1972.
- [167] C. Adloff et al. Measurement of leading proton and neutron production in deep inelastic scattering at HERA. *Eur. Phys. J. C*, 6:587–602, 1999.
- [168] Boris Kopeliovich, Bogdan Povh, and Irina Potashnikova. Deep inelastic electroproduction of neutrons in the proton fragmentation region. *Z. Phys. C*, 73:125–131, 1996.
- [169] Nikolai N. Nikolaev, W. Schafer, A. Szczurek, and J. Speth. Do the E866 Drell-Yan data change our picture of the chiral structure of the nucleon? *Phys. Rev. D*, 60:014004, 1999.
- [170] Krzysztof J. Golec-Biernat, J. Kwiecinski, and A. Szczurek. Reggeon and pion contributions in semiexclusive diffractive processes at HERA. *Phys. Rev. D*, 56:3955–3960, 1997.
- [171] Yu.M. Kazarinov, B.Z. Kopeliovich, L.I. Lapidus, and I.K. Potashnikova. Triple Regge Phenomenology in the Reaction  $p + p \rightarrow p + X$ . *Sov. Phys. JETP*, 43:598, 1976.
- [172] U. D’Alesio and H.J. Pirner. Target fragmentation in  $pp$ ,  $ep$  and  $\gamma p$  collisions at high-energies. *Eur. Phys. J. A*, 7:109–119, 2000.
- [173] V.G.J. Stoks and T.A. Rijken. Soft core baryon baryon potentials for the complete baryon octet. *Phys. Rev. C*, 59:3009–3020, 1999.
- [174] E.A. Hawker et al. Measurement of the light anti-quark flavor asymmetry in the nucleon sea. *Phys. Rev. Lett.*, 80:3715–3718, 1998.
- [175] B Adams et al. COMPASS++/AMBER: Proposal for Measurements at the M2 beam line of the CERN SPS Phase-1: 2022-2024. Technical Report CERN-SPSC-2019-022. SPSC-P-360, CERN, Geneva, May 2019. The collaboration has not yet constituted itself, thus instead of a Spokesperson currently the nominated Contact Person (Jan Friedrich) is acting in place.
- [176] Xurong Chen, Feng-Kun Guo, Craig D. Roberts, and Rong Wang. Selected Science Opportunities for the EicC. *Few Body Syst.*, 61(4):43, 2020.
- [177] Collection et al. EIC Yellow Report. 2021.
- [178] Richard Trotta. EIC Meson MC. [https://github.com/JeffersonLab/EIC\\_mesonMC/tree/master](https://github.com/JeffersonLab/EIC_mesonMC/tree/master), 2020.

- [179] J. Volmer et al. Measurement of the Charged Pion Electromagnetic Form-Factor. *Phys. Rev. Lett.*, 86:1713–1716, 2001.
- [180] T. Horn et al. Determination of the Pion Charge Form Factor at  $Q^2 = 1.60$  and  $2.45$   $(\text{GeV}/c)^2$ . *Phys. Rev. Lett.*, 97:192001, 2006.
- [181] V. Tadevosyan et al. Determination of the pion charge form factor for  $Q^2 = 0.60$ – $1.60$   $\text{GeV}^2$ . *Phys. Rev. C*, 75:055205, 2007.
- [182] H.P. Blok et al. Charged pion form factor between  $Q^2=0.60$  and  $2.45$   $\text{GeV}^2$ . I. Measurements of the cross section for the  $^1\text{H}(e, e'\pi^+)n$  reaction. *Phys. Rev. C*, 78:045202, 2008.
- [183] G.M. Huber et al. Separated Response Function Ratios in Exclusive, Forward  $\pi^\pm$  Electroproduction. *Phys. Rev. Lett.*, 112(18):182501, 2014.
- [184] G.M. Huber et al. Separated Response Functions in Exclusive, Forward  $\pi^\pm$  Electroproduction on Deuterium. *Phys. Rev. C*, 91(1):015202, 2015.
- [185] R.L. Gluckstern. Uncertainties in track momentum and direction, due to multiple scattering and measurement errors. *Nucl. Instrum. Meth.*, 24:381–389, 1963.
- [186] Tom Vrancx and Jan Ryckebusch. Charged pion electroproduction above the resonance region. *Phys. Rev. C*, 89(2):025203, 2014.
- [187] S. R. Amendolia et al. A Measurement of the Pion Charge Radius. *Phys. Lett. B*, 146:116–120, 1984.
- [188] S. R. Amendolia et al. A Measurement of the Space - Like Pion Electromagnetic Form-Factor. *Nucl. Phys. B*, 277:168, 1986.
- [189] H. Ackermann, T. Azemoon, W. Gabriel, H. D. Mertiens, H. D. Reich, G. Specht, F. Janata, and D. Schmidt. Determination of the Longitudinal and the Transverse Part in  $\pi^+$  Electroproduction. *Nucl. Phys. B*, 137:294–300, 1978.
- [190] P. Brauel, T. Canzler, D. Cords, R. Felst, Guenter Grindhammer, M. Helm, W. D. Kollmann, H. Krehbiel, and M. Schadlich. Electroproduction of  $\pi^+n$ ,  $\pi^-p$  and  $K^+\Lambda$ ,  $K^+\Sigma^0$  Final States Above the Resonance Region. *Z. Phys. C*, 3:101, 1979.
- [191] G. M. Huber, D. Gaskell, T. Horn, et al. Measurement of the Charged Pion Form Factor to High  $Q^2$  and Scaling Study of the L/T-Separated Pion Electroproduction Cross Section at 11 GeV. Jefferson Lab 12 GeV Experiment E12-19-006.

- [192] A. P. Bakulev, K. Passek-Kumericki, W. Schroers, and N. G. Stefanis. Pion form-factor in QCD: From nonlocal condensates to NLO analytic perturbation theory. *Phys. Rev. D*, 70:033014, 2004. [Erratum: *Phys.Rev.D* 70, 079906 (2004)].
- [193] W. Melnitchouk. Quark hadron duality in electron pion scattering. *Eur. Phys. J. A*, 17:223–234, 2003.
- [194] V. A. Nesterenko and A. V. Radyushkin. Sum Rules and Pion Form-Factor in QCD. *Phys. Lett. B*, 115:410, 1982.
- [195] Clayton S. Mello, J. P. B. C. de Melo, and T. Frederico. Minkowski space pion model inspired by lattice QCD running quark mass. *Phys. Lett. B*, 766:86–93, 2017.
- [196] Tae Keun Choi, Kook Jin Kong, and Byung Geel Yu. Pion and proton form factors in the regge description of electroproduction  $p(e, e'\pi^+)n$ . *Journal of the Korean Physical Society*, 67(7):1089–1094, Oct 2015.
- [197] M. Carmignotto et al. Separated Kaon Electroproduction Cross Section and the Kaon Form Factor from 6 GeV JLab Data. *Phys. Rev. C*, 97(2):025204, 2018.
- [198] R.M. Mohring et al. Separation of the longitudinal and transverse cross sections in the  $^1\text{H}(e, e'K^+)\Lambda$  and  $^1\text{H}(e, e'K^+)\Sigma^0$  reactions. *Phys. Rev. C*, 67:055205, 2003.
- [199] M. Coman et al. Cross sections and Rosenbluth separations in  $^1\text{H}(e, e'K^+)\Lambda$  up to  $Q^2 = 2.35 \text{ GeV}^2$ . *Phys. Rev. C*, 81:052201, 2010.
- [200] J.R. Oppenheimer et al. Strange particles and weak interactions. In *7th Annual Rochester Conference on High energy nuclear physics*, pages IX.1–52, 1957.
- [201] T. Yamanaka. Detection of a strange particle. *Nature*, 575:36–38, 2019.
- [202] Hideki Yukawa. On the interaction of elementary particles. *Proc. Phys. Math. Soc. Jap.*, 17:48–57, 1935.



**Contents**

<b>1</b>	<b>Introduction</b>	<b>4</b>
1.1	Mass budgets . . . . .	4
1.2	EIC context . . . . .	7
<b>2</b>	<b>Meson structure as a QCD laboratory - status and prospects</b>	<b>8</b>
2.1	Pion and kaon structure - theory status . . . . .	8
2.2	Pion and kaon Structure - lattice QCD status . . . . .	14
2.3	Global QCD analysis . . . . .	18
2.4	Synergy between theory calculations and data analysis . . . . .	20
<b>3</b>	<b>Key EIC measurements</b>	<b>24</b>
3.1	Sullivan process . . . . .	25
3.2	Theoretical backgrounds in extracting the data . . . . .	26
3.3	Kinematics of interest to address specific theory questions . . . . .	30
3.4	Complementarity with other facilities . . . . .	31
<b>4</b>	<b>Kinematic coverage and detector requirements</b>	<b>32</b>
4.1	Far-forward area setup. . . . .	32
4.2	$e p \rightarrow e' + X + n$ . . . . .	33
4.3	$\Lambda$ tagging . . . . .	34
4.4	Exclusive $p(e, e'\pi^+n)$ events . . . . .	42
4.5	Accelerator and instrumentation requirements . . . . .	44
<b>5</b>	<b>Physics projections</b>	<b>45</b>
5.1	Meson structure functions . . . . .	45
5.2	Meson form factors . . . . .	49
<b>6</b>	<b>Summary and prospects</b>	<b>53</b>